in the central collision of two heavy nuclei as a function of the bombarding energy [Bau75, Stö78]. This model assumes the compressed fluid to be at rest in the center of momentum system (equal velocity frame). Three dimensional fluid dynamical calculations show that this requirement is fulfilled fairly well for non-peripheral collisions of heavy nuclei near the collision axis: A quasi-stationary compression stage develops. That means, that practically all of the incident kinetic energy is transformed into internal energy (compression and excitation). As v_f denotes the flow velocity of the shocked matter, which is at rest in the c.m. frame, relative to the target matter, we can calculate the laboratory bombarding energy via

$$E_{\text{Lab}} = [(1 - (v_p/c)^2)^{-1/2} - 1]W_0 \tag{II.92}$$

where $v_p = 2v_f/(1 + (v_f/c)^2)$ is the projectile velocity.

Though this model will, due to the lack of kinetic energy of the compressed matter and due to the outflow of matter perpendicular to the collision axis, give too large values for compression and temperatures as a function of the bombarding energy (as compared to three dimensional calculations), it is sufficient to give an overview about the expected compression and thermal excitation. The influence of the beam energy and the nuclear equation of state (e.g. different compressibility constants) and the importance of resonance and pion production in the collision dynamics can thus be studied nearly analytically.

III. Confrontation of the Theory with Experimental Data – Extraction of the Nuclear Equation of State

III.1. Expansion, fragment formation and the entropy puzzle

III.1.1. Compression and expansion

In the preceding chapter the fluid dynamical model has been introduced. Historically fluid dynamics has been the first approach to be applied to high energy nuclear collisions. This model is most intuitive in that it refers directly to the thermodynamical concepts developed in chapter I. Therefore the underlying physics of high compression and excitation can be discussed in a macroscopic language. The spatial and temporal distributions of the density, velocity, temperature, etc. as obtained from this approach are analyzed in the following. The dependence of the thermodynamic variables on the impact parameter, bombarding energy, and projectile–target combination is studied. The fluid dynamical model is the only one of the above discussed approaches for which the nuclear equation of state serves as immediate input – the VUU approach also includes the compression energy, but since it is a non-equilibrium theory the statistical variables temperature, thermal pressure, etc. are not easily accessible. We use the fluid dynamical model in the following as a reference case – not only to compare to the data, but also to the microscopic theories.

The fluid dynamical development of a heavy ion collision typically proceeds in the following way (fig. III.1): When two nuclei collide at high energy the overlap zones are stopped and a strong non-linear shock wave is formed. High density, pressure and temperature are created in this region. This stage is described by the "compression" line in fig. III.1. The numbers on that line indicate the energies in GeV/n at which the corresponding maximum values for ρ/ρ_0 and T are reached. At $E_{\text{Lab}} = 200$ MeV/n, for example, a maximum compression of three times equilibrium density and a temperature of about 40 MeV can be obtained. During that stage the entropy of the system rises up to a certain saturation

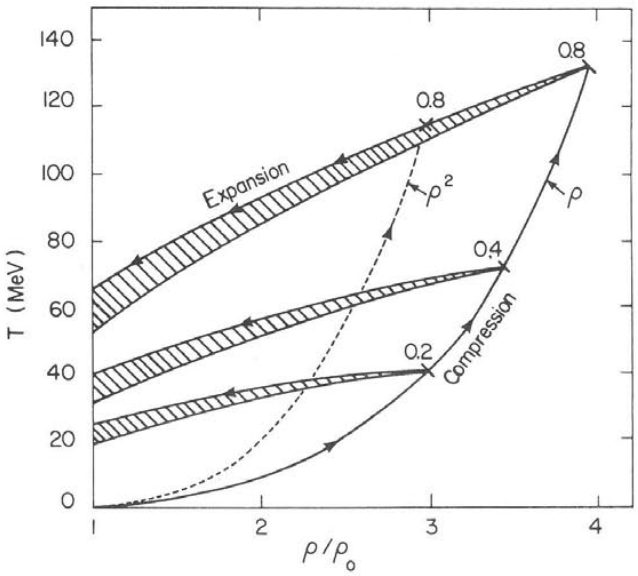

Fig. III.1. Path of the dynamics of nuclear collisions in the ρ–T phase diagram showing the compression Hugoniot adiabat and isentropic expansion stage. The influence of the compressional energy is depicted by the solid line (linear EOS) and the dashed line (quadratic EOS) – clearly the compression achievable depends quite strongly on the repulsive short range interactions [Stö84a].

value which depends on the nuclear equation of state, the bombarding energy and the viscosity in the system.

Subsequent to this compression phase the temperature drops during the hydrodynamic (quasi-adiabatic) expansion while the entropy S stays nearly constant at the asymptotic value reached at the point of highest compression. A three dimensional calculation of the entropy is shown in fig. III.2 [Buc86] – observe that the entropy is increased somewhat due to viscous effects [Cse80, Stö84, Buc84]. The system expands due to its large internal pressure and at densities $\rho \sim 0.5$–$0.7\,\rho_0$ the collisions between the particles cease: the hydrodynamic description loses its validity and the nuclear fluid breaks up into light fragments π, p, n, d, He, ... The fragments formed in this late stage of the reaction are the only messengers from the reaction which are actually observed experimentally. Fragment formation is a topic of great current interest because of their possible relation to the entropy and also in connection with speculations about the discovery of the nuclear liquid–gas phase transition [Stö83, Cse85, Hah86].

In the fluid dynamical model the fragment formation is usually treated in the quantum statistical approach presented below. The fragments carry the only available information from the initial dense state of the system. However, they have gone through the much later freeze-out stage which follows the hydrodynamical expansion of the reaction. This freeze-out starts when the density in the fluid becomes so low that the particles in the fluid cease to interact – then the fluid breaks apart into single fragments. The quantum statistical model used to obtain the fragment yields and the spectra is described in the next paragraph.

III.1.2. Quantum statistical model of break-up and fragment formation

We will in the following concentrate on the formation of light and medium mass fragments in the

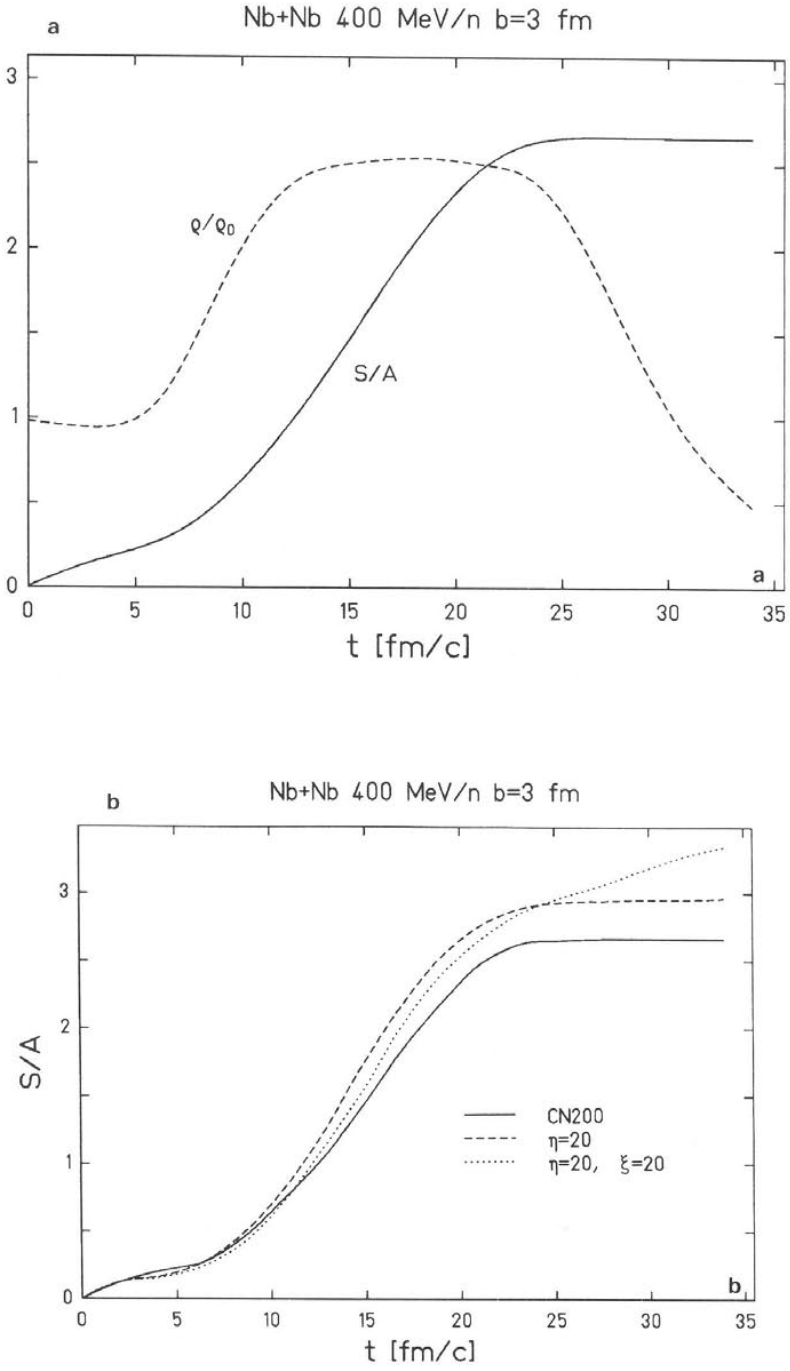

Fig. III.2. Shows the time dependence of the entropy production as obtained with the three dimensional viscous fluid dynamical approach [Buc86] for the reaction Nb (400 MeV/nucleon) + Nb at $b = 3$ fm. (a) compares the maximum density with the entropy: entropy is produced during the high density stage of the reaction. The entropy stays constant during the expansion, therefore the entropy can be used as a messenger from the high density stage. (b) inclusion of viscous effects modifies the entropy: shear viscosity only (dashed line) raises the total entropy, bulk viscosity (dotted line) destroys the saturation of $S/A(t)$ observed in the other cases.

freeze-out stage of the collision. There are two important questions: What is the "chemical" composition of the reaction products, i.e. how abundant and where are the different nuclei, π etc. produced? What is their distribution in momentum space, i.e. what do the experimentally observed spectra look like? These two points are discussed in the following section.

To simulate the transition from the interacting nucleon fluid to the free gas of nuclear fragments traveling towards the detectors the hydrodynamic calculation is halted when the average density is $\approx 0.5\rho_0$. Then the light fragment composition is calculated from a quantum statistical model by assuming that the baryon number and energy per particle of the interacting nucleon fluid is conserved. The quantum statistical model [Gos78, Sub81, Stö83, Hah85] used to calculate the fragment yields assumes that chemical equilibrium between the different fragments produced (p, n, d, t, ^{3}He and α's...) is established towards this late stage of the collisions. This assumption is supported by rate calculations for the appropriate densities and temperatures [Mek78].

The model can be recapitulated as follows [Sub81]: Baryon number and charge conservation are enforced via

$$\bar{Z} = \sum_{i=1}^{N} n_i(Z_i, N_i) \cdot Z_i \tag{III.1}$$

$$\bar{N} = \sum_{i=1}^{N} n_i(Z_i, N_i) \cdot N_i \tag{III.2}$$

where n_i is the number of particles of species i with Z_i protons and N_i neutrons. The equilibrium is established in a volume V_{ext} (or at a density ρ) and at a temperature T. Every particle moves freely in the volume V left over from the external volume V_{ext} after subtracting the volume occupied by each particle,

$$V = V_{\text{ext}} - \sum_i n_i V_i\,, \qquad \rho = (\bar{N} + \bar{Z})/V_{\text{ext}} \tag{III.3}$$

where V_i is the ith particle's volume. So the point-like particles move freely in a reduced volume V with the point particle density determining the chemical equilibrium of $\rho_{\text{pt}} = (\bar{N} + \bar{Z})/V$. For fermions we have

$$\lambda_1^3 N_i/g_i V = (2/\pi^{1/2}) F_{\text{FD}}(\nu_i)\,, \qquad i = \text{p, n, }^3\text{He, t, } \ldots \tag{III.4}$$

where

$$\lambda_i = h/(2\pi m_i kT)^{1/2} \tag{III.5}$$

is the thermal wavelength of the ith particle with mass m_i. The spin degeneracy factor $g_i = 2S_i + 1$. The chemical potential of the ith particle is μ_i,

$$\nu_i = \beta\mu_i = \mu_i/kT \tag{III.6}$$

and

$$F_{\mathrm{FD}}(\nu) = \int_0^\infty \mathrm{d}x\, x^{1/2}/(\exp(x-\nu)+1)\,. \tag{III.7}$$

The function $F_{\mathrm{FD}}(\nu)$ is tabulated in the literature [Sub81]. For bosons we have

$$N_i = 1/(\exp(\alpha_i)-1) + (g_i V/\lambda_i^3)\, F_{\mathrm{BE}}(\alpha_i)\,, \qquad i = \mathrm{d}, {}^4\mathrm{He}, \ldots \tag{III.8}$$

where $\alpha_i = -\beta\mu_i$, the final term gives the number of condensed particles, and

$$F_{\mathrm{BE}}(\alpha) = \sum_{n=1}^{\infty} \exp(-n\alpha)/n^{3/2}\,. \tag{III.9}$$

The constraint of chemical equilibrium implies that the chemical potential

$$\mu_i = Z_i\mu_{\mathrm{p}} + N_i\mu_{\mathrm{n}} + E_i \tag{III.10}$$

where

$$E_i = Z_i m_{\mathrm{p}}c^2 + N_i m_{\mathrm{n}}c^2 - m_i c^2 \tag{III.11}$$

is the binding energy of the cluster (Z_i, N_i).

III.1.3. Thermal fragment emission

The particle cross sections are calculated by transforming the internal thermal momentum distribution for each particle density in every fluid element to the laboratory system with the corresponding flow velocity [Cse80, Buc81, Cse83]. The inclusive cross sections are obtained by a weighted average over the impact parameter.

The thermal momentum distribution of the nucleons inside a fluid cell is described by relativistic Fermi distributions. To obtain the momentum distribution of all fragments in the laboratory frame the distributions are Lorentz transformed to this frame by the relativistic boost velocity β_j of the cell j arising from the collective flow [Cse80, Buc81]:

$$f_j^{\mathrm{lab}}(\boldsymbol{P})\,\mathrm{d}^3\boldsymbol{P} = \frac{w(\boldsymbol{P})}{W} f_j[\boldsymbol{P}(\boldsymbol{p})]\,\mathrm{d}^3\boldsymbol{P}\,. \tag{III.12}$$

Here $(\frac{w}{p})$ and $(\frac{W}{P})$ are the four-momenta in the cell and lab systems, respectively. From eq. (III.12) we obtain the double differential cross section of the emitted fragments via

$$\frac{\mathrm{d}^2\sigma}{\mathrm{d}W\,\mathrm{d}\Omega} = \sum_j \frac{4V_j\sigma_0}{(2\pi\hbar)^3} \frac{A_j(W^2-m^2)^{1/2}}{\exp[(A_j-\mu_j)/T]+1} N_{\mathrm{particle}} \tag{III.13}$$

where V_j is the volume of the corresponding fluid cell, σ_0 is the geometrical cross section of the reaction, and

$$A_j = \gamma_j (W - \boldsymbol{\beta}_j \boldsymbol{P}_j) \,. \tag{III.14}$$

N_{particle} is the fraction of the corresponding particle species calculated in the chemical equilibrium mode from above. The momentum vector p of the observed particle depends on the observation energy E and angles θ and ϕ:

$$\boldsymbol{p} = (W^2 - m^2)^{1/2} \begin{pmatrix} \sin\theta\cos\phi \\ \sin\theta\sin\phi \\ \cos\theta \end{pmatrix}, \tag{III.15}$$

where $W = m + E$. This method is applied below to calculate fragment spectra and angular distributions from the fluid dynamical model.

III.1.4. Light fragments and the entropy puzzle

Since – as seen in fig. III.2 – for a perfect fluid the entropy saturates at its asymptotic value already in the moment of highest compression and stays constant during the expansion from this compressed state, a method that would allow to determine the entropy from experiment could yield important insight into the state of the matter in the moment of highest compression and excitation of the collision.

It has been suggested [Sie79] to measure the entropy S via the observed deuteron-to-proton ratio R_{dp}: In chemical equilibrium

$$S = 3.95 - \ln R_{\text{dp}} \qquad [\text{for } \langle p \rangle_{\text{equil.}} \gg \langle d \rangle_{\text{equil.}}] \,. \tag{III.16}$$

This formula has been used to extract entropy values from the inclusive fragment data [Nag81]. The resulting entropy values are plotted in fig. III.3 as a function of the bombarding energy. Also shown are the entropy values obtained from the hydrodynamical model [Stö84].

The experimental values of S seem to be much larger than the calculated entropy values, in particular for $E_{\text{Lab}} \leq 400$ MeV/n, even after the effects of viscosity are considered. However, the neutron-to-proton ratios calculated from fluid dynamics with an attached quantum statistical model, $R_{\text{dp}} < 0.35$, agree well with the experimental data over the whole range of bombarding energies considered [Nag81] (see fig. III.4). This paradox is resolved [Stö84] as being due to the decay of the particle unstable excited nuclei,

$$A^* \rightarrow (A-1) + \text{p} \,, \tag{III.17}$$

which become increasingly important at intermediate and low energies [Stö84]. In fact, the resonance decay products dominate the chemical equilibrium contribution for $E_{\text{Lab}} < 400$ MeV/n. Hence the relation between the entropy and the observables is not given by the simple formula given above. It turns out, however, that the entropy can be related to the d to p ratios discussed above in the quantum statistical model whence the decay of particle unstable states is explicitly included. The relation to the entropy is then not given via the simple equation (III.16), but has to be determined from a full numerical quantum statistical model calculation of several hundred stable and unstable nuclides (see fig. III.5). Recent data from the GSI/LBL Plastic Ball collaboration have made clear, though, that the d to p ratio depends strongly on the multiplicity of the event in which the particles are emitted: in peripheral collisions,

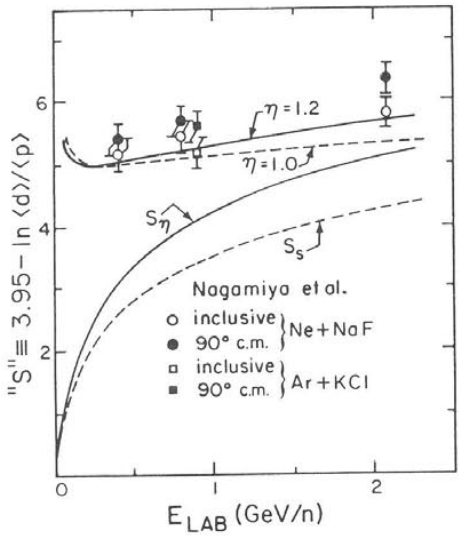

Fig. III.3. Dependence of the entropy per baryon on the bombarding energy. S_s (dashed line): result of a one dimensional shock calculation; S_η (solid line): entropy production with viscous effects included; "data": estimate of the entropy production obtained from the simple relation (eq. (III.16)) given by Siemens and Kapusta [Sie79], and prediction of fluid dynamics with attached quantum statistical model of fragment production [Stö84a].

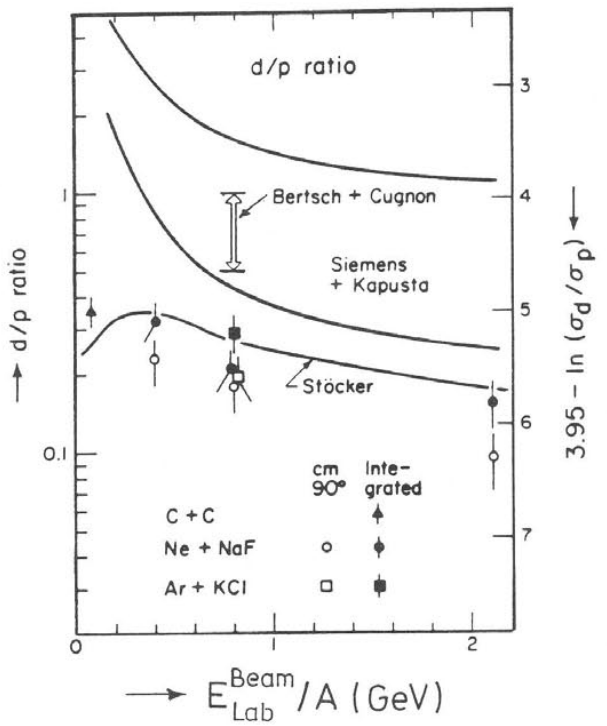

Fig. III.4. Bombarding energy dependence of the d/p ratios as obtained from inclusive measurements and various theoretical approaches. The calculations of Bertsch and Cugnon, as well as Siemens and Kapusta grossly overestimate the data [Nag81].

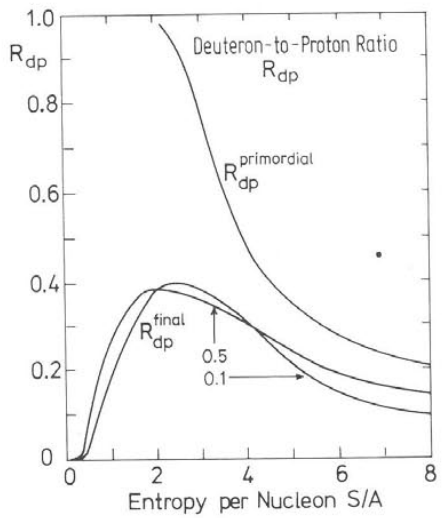

Fig. III.5. Quantum statistical model prediction of the dependence of the d/p ratio on the entropy. The primordial d/p ratio (upper line) is strongly distorted by the decay of particle unstable nuclear and hadronic resonances [Stö83].

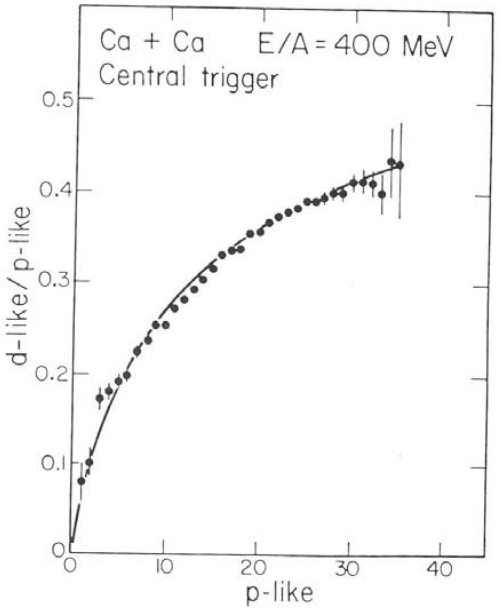

Fig. III.6. Multiplicity dependence of the d/p ratio as observed in the Plastic Ball 4π electronic spectrometer system [Gus84b]. This result indicates that inclusive measurements are not suitable for an extraction of the entropy – the thermodynamic lines can only be approached for very high multiplicities, i.e. very massive colliding nuclei.

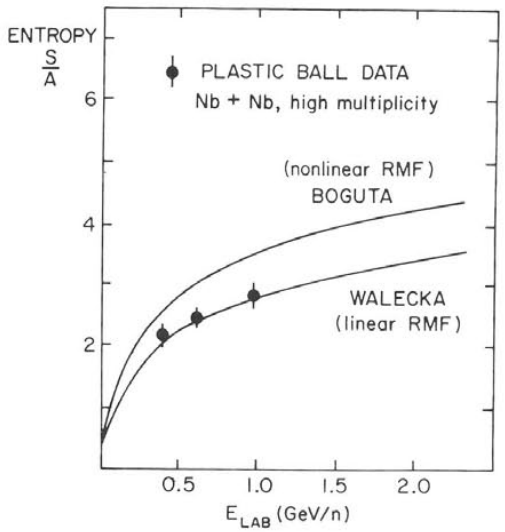

Fig. III.7. Extraction of the entropy from the high multiplicity Plastic Ball data for heavy systems [Gus84b, Dos85]. A surprisingly low entropy is obtained if the quantum statistical model is applied [Hah85]. The data are compared to fluid dynamical calculations which use different relativistic mean field theories as input for the equation of state [Stö81a].

which dominate the inclusive particle spectra, the ratio is much smaller than in central collisions with high multiplicity (see fig. III.6) [Gus85]. The quantum statistical model has been used to extract the entropy from the asymptotic (infinite multiplicity) 'data' [Dos85]. The results are shown in fig. III.7 in comparison with the entropy values calculated in the fluid dynamical model with a stiff and a soft nuclear equation of state [Stö81]. We want to emphazise that the data are in strong disagreement with the fireball calculations – they seem to indicate strong compression effects and point towards a stiff nuclear equation of state.

III.1.5. Temperatures and single particle spectra

The temperatures T as calculated in the hydrodynamical model [Stö81] are compared in fig. III.8 to the experimentally determined slope factors T_0 [Nag81] of protons and pions emitted from violent nuclear collisions at various bombarding energies. The data seem to rule out a pure nucleon Fermi gas (dashed curve) at energies $E_{\mathrm{Lab}} > 800$ MeV/n. A mixture of non-interacting gases of the different hadrons with an exponentially increasing hadronic mass spectrum (solid curves) seems to be in much better agreement with the data.

However, it has to be pointed out that the finally observed slope factors do not give a direct measure of the initial temperature: Due to the expansion the temperature drops substantially [Stö81]. This is compensated by an increase in the collective flow velocity. It is interesting that those effects roughly balance each other because of energy conservation and the finally obtained slopes of the spectra do not deviate too strongly from the initial temperature.

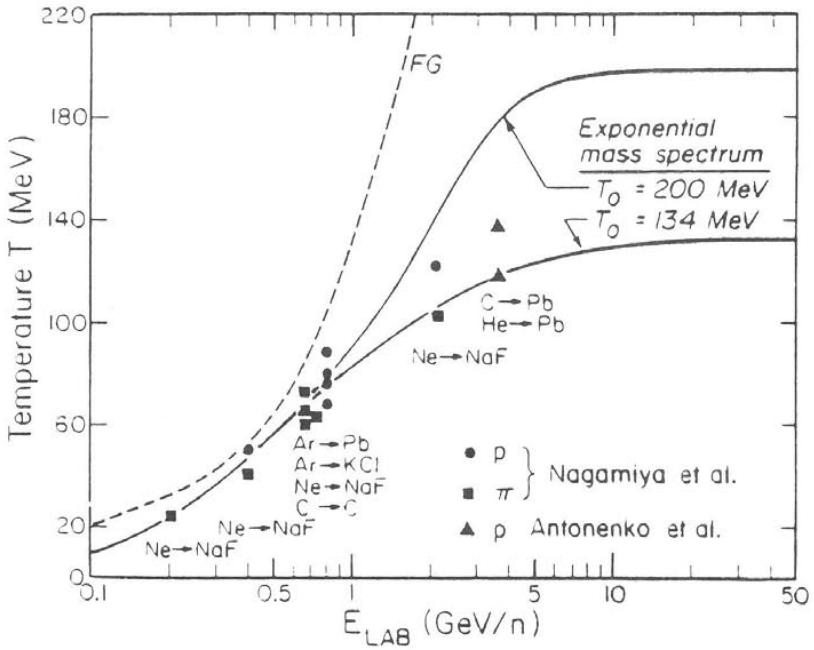

Fig. III.8. Bombarding energy dependence of the temperature calculated in the shock model using different equations of state: nucleon Fermi gas (dashed line) and hadron plasma with a Hagedorn mass spectrum [Stö81c]. The data are extracted from fits to the 90° c.m. slopes of the spectra of protons (and pions) [Nag81].

III.2. Pion production and the nuclear compression energy

The nuclear fluid dynamical model can also be used to predict pion yields and study their dependence on the nuclear equation of state [Stö78, Dan79, Hah85]. Figure III.9 shows the original calculation of Stöcker, Scheid and Greiner, who first proposed to measure the stiffness of the nuclear compression energy via the pion multiplicities. The first exclusive measurements of the pion multiplicities as a function of the participant multiplicity is shown in fig. III.10 [San80]. It has been used recently to extract the compressional energy via the method proposed [Stö78, Har85, Hah85, see fig. III.11] and via a subtraction procedure, which used the cascade model – which does not employ any compressional energy – as input [Sto82]. It turns out that the data can only be explained if a very stiff compression potential is assumed [see fig. II.3]. The assumption of immediate freeze-out in the high density stage in this procedure could overestimate the pion multiplicities, which would drop during an isentropic expansion of the system before freeze-out [Stö81c, 84c] (see fig. III.10). However, cascade calculations show that the pion degree of freedom decouples from the baryonic 'heat bath' very early in the collision, namely in the high density stage [Cug80, Sto82].

To study pion production on the microscopic level the VUU theory can be employed [Kru85, Mol85]. Pions of different isospin are produced in this model via a delta resonance mechanism in elementary nucleon–nucleon collisions: thus both production and absorption mechanisms are treated microscopically. The VUU approach has first been tested by turning off the Pauli blocking and mean potential field. Then the parallel ensembles decouple and the test particles move on straight line trajectories until they scatter – thus the intranuclear cascade model is recovered. The pion yields calculated with the VUU method in the cascade model agree quantitatively with results obtained with the

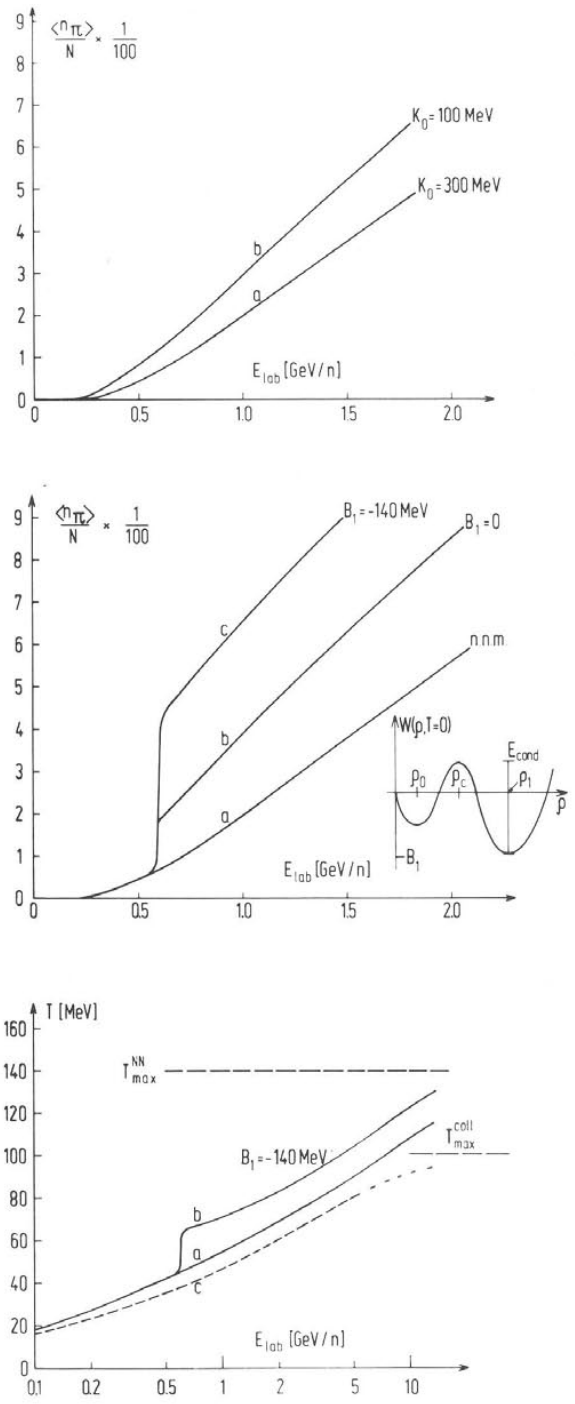

Fig. III.9. Early predictions on the bombarding energy dependence of the pion multiplicities and their dependence on the nuclear compressional energy [Stö78]. The upper frame shows the influence of the compression constant, using the linear $E_C(\rho)$ ansatz. The middle frame shows the influence of a hypothetical abnormal density isomeric state; threshold increase of pion production is predicted at a critical energy. Lowest frame: influence of the EOS on the temperature achieved in shock compression.

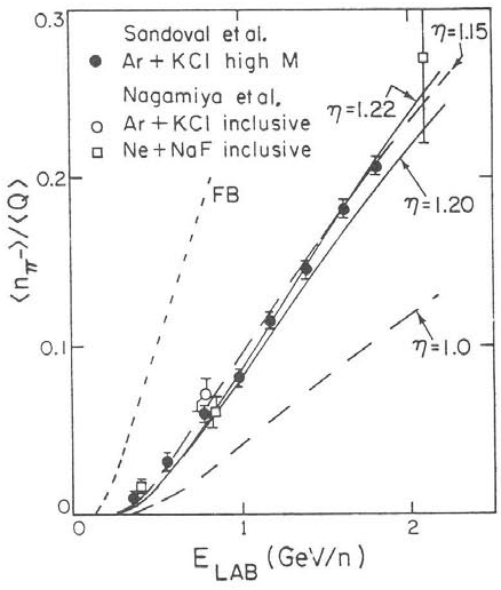

Fig. III.10. The observed pion multiplicities [San80] are compared to fireball calculations (short dashed line) and non-viscous fluid dynamics with late freeze-out (long dashed line). The influence of the viscosity is shown by the lines labeled η[Stö84a].

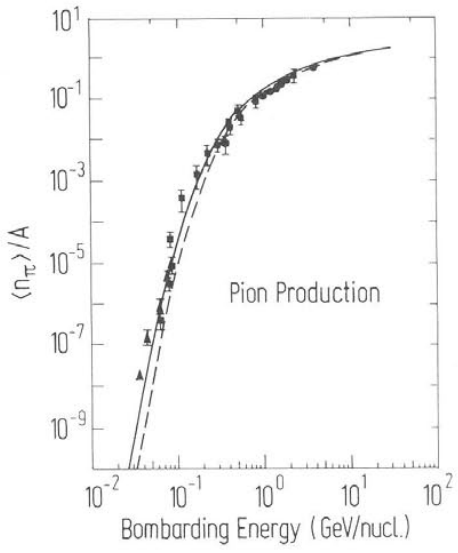

Fig. III.11. Pion multiplicities per nucleon versus bombarding energy calculated with the shock model with the quadratic EOS and $K_q = 250$ (solid) and 500 (dashed) MeV, respectively [Hah86].

conventional cascade, e.g. of Cugnon et al. and Yariv et al. [Cug80, Yar81]. Both results differ substantially from the data. If the nuclear compression energy and the Pauli blocking are employed in the VUU-method, the pion multiplicities change dramatically, as shown in fig. III.12 [Kru85]: Take the 360 MeV/nucleon case, for instance. The π^- yield is 1.05 in the cascade mode, but drops to 0.56 if the compression energy is included; the suggested large difference due to the nuclear matter EOS is

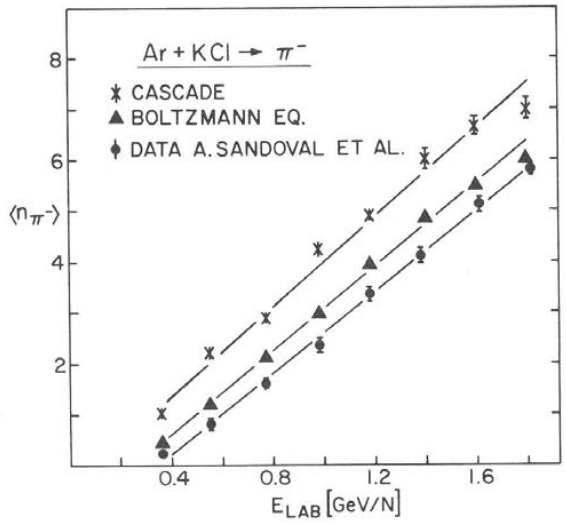

Fig. III.12. π^--multiplicity versus energy for the system Ar + KCl in the cascade approach [Cug80] and VUU theory [Kru85a] as compared to the experimental data [San80].

observed. The pion yield drops further to 0.46 when the VUU Pauli blocking is applied. These results differ by factors of three from results published elsewhere [Ber84a]; a revised version of that program [Aic85b] now reproduces the results presented here.

The pion multiplicities as calculated with the full VUU theory are shown in fig. III.12 as a function of the bombarding energy for the Ar + KCl system. The VUU theory with stiff EOS plus phase space Pauli blocker compares well with the data whereas the cascade mode overestimates the data by factors >2 at energies up to 1 GeV/nucleon, just like the intra-nuclear cascade calculations.

The required drop in the predicted pion yield is found to be due to the transformation of kinetic energy into potential energy during the high density phase of the reaction as well as due to Pauli blocking. To check the sensitivity of the pion yields to the EOS the calculations have been repeated with the medium potential. At 772 MeV/nucleon we find $n_{\pi^-} = 2.45$ and 2.13 with the medium and the stiff EOS respectively. At lower energies, statistical error bars of 10% preclude an accurate assessment of the effect of the potential. At all other energies, where the error bars are 3%, the yields are systematically higher by about 10% with the medium EOS. The stiff equation of state which reproduces the pion yields best is shown in fig. II.3 together with the medium EOS. We will confront these equations of state with other data on nuclear flow below. We want to announce here already that we will find further support for the stiff equation of state also from these completely independent comparisons.

The time dependence of the total pion multiplicity as calculated from the VUU approach for Nb (1050 MeV/nucleon) + Nb collisions at $b = 3$ fm is shown in fig. III.13a [Mol85]. Note that the pion number rises rapidly to a maximum value at 10 fm/c and then drops to a stable final value by 20 fm/c. There is a small but significant effect due to re-absorption until the pions escape from the hot interaction zone. We want to emphazise that in this theory – as in the previously discussed cascade calculations – the pion yield approaches its asymptotic value at a time which nearly coincides with the moment of highest compression (fig. III.13b) and 'temperature', thus demonstrating one more time that information on the high density stage can be obtained.

The bombarding energy dependence of the total pion multiplicity at $b = 3$ fm for Nb + Nb collisions is shown in fig. III.14a. For the system Au + Au, the pion multiplicity for $b = 3$ fm collisions is shown in fig. III.14b for the different isospin channels in the final state. Note that the VUU theory predicts a distinct difference of the pion multiplicity with a charged pion ratio $\pi^-/\pi^+ \approx 2$.

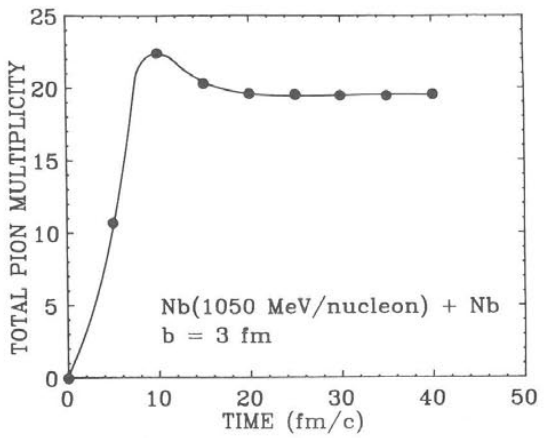

Fig. III.13a. The total pion multiplicity versus time in the VUU approach for Nb (1050 MeV/nucleon) + Nb at $b = 3$ fm; note the small but significant effect of re-absorption [Mol85].

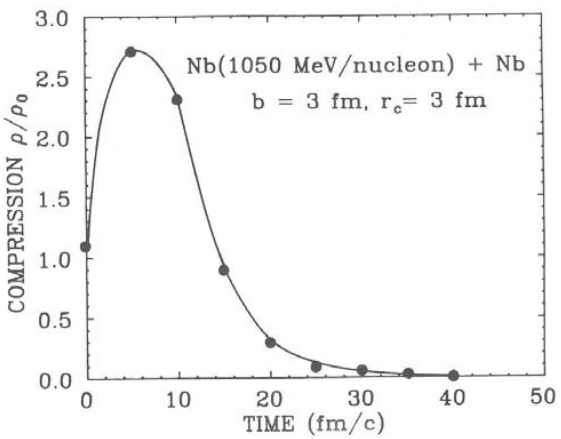

Fig. III.13b. The corresponding figure for the maximum density achievable: pions can serve as signals from the high density stage [Mol85].

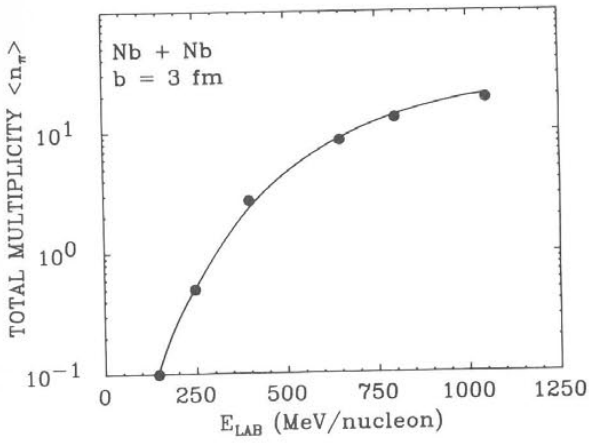

Fig. III.14a. Total pion multiplicity versus bombarding energy for Nb + Nb at $b = 3$ fm in the VUU theory [Mol85].

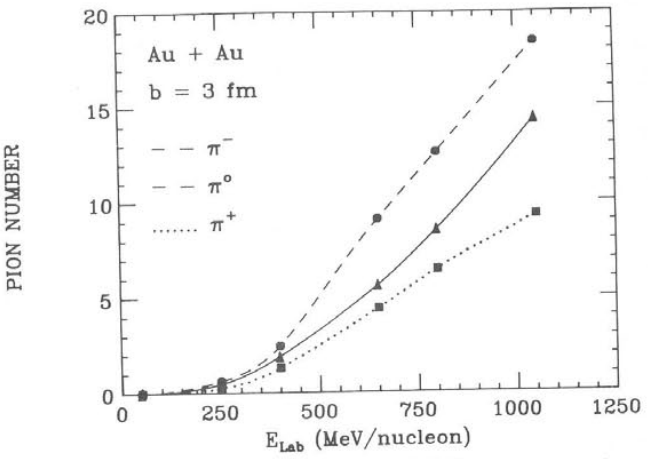

Fig. III.14b. VUU predictions for pion multiplicities versus energy for Au + Au at $b = 3$ fm. Note the strong influence of isospin [Mol85].

The VUU approach has also been used to study pion production in asymmetric nucleus–nucleus collisions [Mol86]. It is observed that in Ar (770 MeV/nucleon) + Pb collisions the pions tend to escape into the backward hemisphere at low impact parameters. At intermediate impact parameters the pion emission pattern is directed sidewards away from the high density zone. The total average pion multiplicities vary from 10.6 at $b = 1$ fm to 3.7 at $b = 7$ fm. About 25–30% more pions are created when the Pauli blocking is turned off. This is understood physically: with the Pauli principle turned off, the final state phase space in the intermediate rapidity region is more strongly occupied; equivalently, with the Pauli principle turned on, many collisions that would otherwise produce pions are forbidden by Pauli blocking.

III.3. Collective sidewards flow – Evidence for shock compression and a hard equation of state

III.3.1. Inclusive fragment spectra

Spectra obtained from the hydrodynamical model by the freeze-out procedure described in paragraphs III.1.2–5 can be compared directly with the experimental observations at various input energies. We would like to point out that little information about the details of the reaction mechanism can be extracted from comparison of the inclusive data and impact parameter averaged calculations. For example, in spite of its obvious presence at small impact parameters, no signatures of the collective sidewards flow predicted by the fluid dynamical calculations for central impact parameters seems to be visible even in the calculated inclusive cross sections [Ams75, Am77, Buc83]: only by triggering for nearly central collisions, i.e., high multiplicity selected events, can the sensitivity of the experiments be improved. Furthermore, since the proton production probability is largest in hot regions [Sub81] the effect of the collective flow is smeared out by the thermal motion, which makes the proton cross sections almost isotropic. This phenomenon has been observed at high energies [Sto80] and seems in agreement with previous three dimensional non-viscous calculations [Stö81b, 82].

A better experimental testing ground for flow effects is therefore provided by particles heavier than the proton, e.g. t, ^{3}He, α (or also Li, Be, C) cross sections. These particles are produced in colder regions of the system [Stö 81b, 82]. Hence, they tend to exhibit the signatures of the collective flow more strongly. In fig. III.15 we compare the calculations [Buc84a, 86] with recent measurements of B.V.

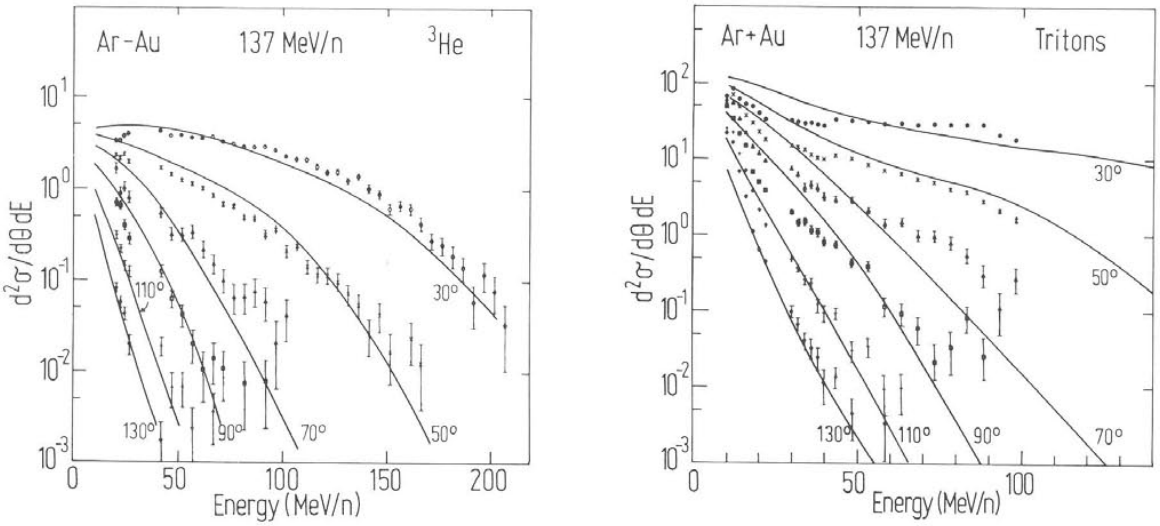

Fig. III.15. Inclusive ^{3}He (left) and triton (right) cross sections from the reaction Ar 137 MeV/n + Au as obtained from nuclear fluid dynamics with the attached quantum statistical model [Buc86] compare well with the data of Jacak et al. [Jac83].

Jacak, G.D. Westfall et al. [Jac83] for ^{40}Ar + ^{197}Au at 137 MeV/N. The left frame shows the inclusive double differential ^{3}He cross section, the right frame compares the results for tritons. In both cases a reasonable agreement can be seen between the calculation (full lines) and the data. Especially the tendency of the ^{3}He spectrum to decrease with decreasing energy and the opposite behavior of the triton spectrum is reproduced fairly well. This systematic behavior is due to the neutron rich Au target, preferring neutron-rich particle production at low energies.

The Ar + Au spectra at lower energies seem to indicate a transition to a different reaction mechanism – whereas the 92 MeV/N data still show a reasonable agreement with the fluid dynamical calculations, there is a clear misalignment for $E_{\mathrm{Lab}} = 42$ MeV/N. Especially at forward angles the data are totally missed by the fluid dynamical calculation, thus indicating that the stopping power of nuclear matter decreases drastically at these low energies.

III.3.2. High multiplicity selected inclusive data

First fingerprints for collective flow have been found in high multiplicity selected early particle track detector experiments [Bau75], which exhibit sidewards maxima in the angular distribution of He – nuclei emitted in very asymmetric reactions, e.g. C + Ag. Also in the double differential cross sections of light fragments (p, d, t) emitted from high multiplicity selected reactions of Ne + U exhibit sidewards maxima, in accord with the longstanding predictions of the nuclear fluid dynamical model [Sch74, Stö80], while the intranuclear cascade model exhibits forward peaking [Stö80]. The angular distributions of protons emitted in central collisions of Ne (393 MeV/N) on U exhibit broad sidewards maxima (middle left frame of fig. III.16). The numbers in the figure indicate the proton kinetic energies. Cascade calculations [Stö81b, 82] yield forward-peaked angular distributions, even if central collisions are selected (upper and lower left frame). Hydrodynamic calculations without thermal break-up yield sidewards peaks which are too narrow (lower right frame) [Stö81b, 82]. The simplified two component and firestreak models (upper right frame) give similar results as the complex three dimensional cascade calculations, thus indicating thermalization in the cascade, but since they are also forward peaked, they also disagree with the data. On the other hand, the fluid dynamical model with final break-up included

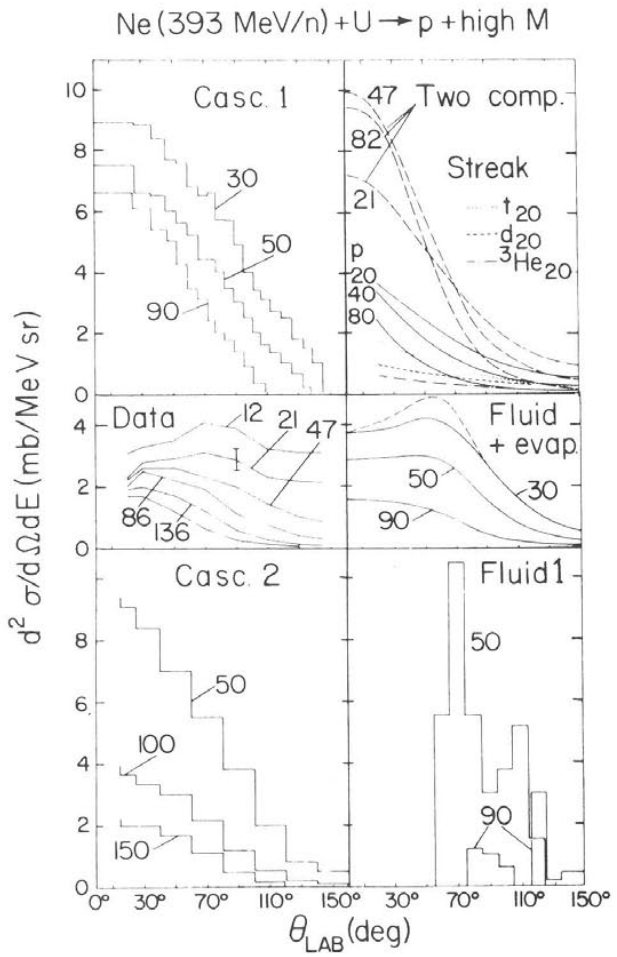

Fig. III.16. Inclusive, but high multiplicity selected proton cross sections from Ne (400 MeV/nucleon) + U exhibit broad sidewards maxima [Sto80] (data: middle left frame). Cascade calculations of Stevenson (lower left) and Yariv and Frankel (upper left) result in strongly forward peaked angular distributions, in agreement with thermal model calculations of Westfall and Schürmann (upper right), but in sharp contrast to the data. Fluid dynamics predicts sharp sidewards maxima [Stö80a, Nix82] if the thermal break-up is not included (lower right frame); the incorporation of thermal evaporation (middle right) yields qualitative agreement of the non-relativistic fluid model with the data [Stö81].

[Stö81b, 82] (middle right frame) gives a reasonable description of the observed forward suppression and also reproduces qualitatively the forward shift of the position of the sidewards maxima with increased proton energy.

However, as the bombarding energy is increased, relativistic effects become increasingly important. The range of validity of the non-relativistic formalism is not sharply defined, but at bombarding energies $E_{\mathrm{Lab}} > 500$ MeV/N, the relative velocity of projectile and target exceeds the speed of light, c, and at best qualitative results may be obtained. In fact, this can already be seen at 400 MeV/N, where the relativistic treatment has a substantial influence on the spectra [Sto80] of protons, deuterons and tritons emitted from central collisions of Ne + U. Figure III.17 shows the comparison of the relativistic calculations [Gra84] with the data [Sto80]. Observe that the agreement with the experimental data is much improved as compared to the non-relativistic calculations presented earlier (fig. III.16). Therefore, the relativistic formulation of the hydrodynamic model is always used in the rest of the article at higher

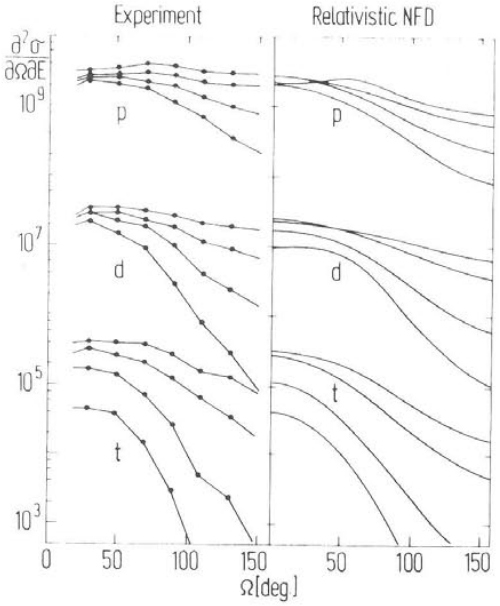

Fig. III.17. High multiplicity selected p, d and t angular distributions as measured by the GSI–LBL collaboration [Sto80] are compared to the relativistic fluid dynamical calculations of the Frankfurt school, which include the quantum statistical calculation of fragment formation plus thermal evaporation of the various ejectiles [Gra84]. The relativistic treatment and the fragment formation prove essential for a quantitative reproduction of the data as compared to the previous qualitative agreement obtained with the earlier non-relativistic calculation [Stö81].

energies, $E_{\mathrm{Lab}} > 0.4$ GeV/N. However, the forward emission of particles is still strongly suppressed exhibiting sidewards maxima. It is important to point out that these sidewards maxima are predicted to be even more pronounced for the summed charges than for protons. In fact, such behavior has been found in experiments with α-particle detectors [Bau75]. Also, the high multiplicity selected angular distributions of ^{2}H and ^{3}H [Sto80] show sharper sidewards peaking than the protons.

The qualitative features of the ϕ-averaged distributions calculated in the fluid model, however, do not change dramatically with impact parameter, once violent collisions with $b \leq 4$ fm are selected. This means, unfortunately, that ϕ-averaged double differential cross sections are of limited value for obtaining information on details of the reaction dynamics and on the nuclear equation of state [Ber78, Stö80b]. Therefore, we next consider whether the azimuthal dependence of the differential cross sections, to be obtained from 4π exclusive experiments with single event analysis [Gus84, 84b, Ren84, Mey80], can provide more specific dynamical information.

III.3.3. Event by event analysis – Triple differential cross sections

Figure III.18 shows the *triple* differential cross sections [Stö82a] $\mathrm{d}^3\sigma/\mathrm{d}\cos\theta\,\mathrm{d}\phi\,\mathrm{d}E$ in the scattering plane, i.e., the rapidity y-transverse momentum p_{T} plane at $\phi = 0°$–$180°$, for the reaction ^{20}Ne (393 MeV/nucleon) + ^{238}U at various impact parameters b. For head-on collisions, $b = 0$ fm, the two maxima at $p_{\mathrm{T}}/m \approx 0.1$–$0.2$ indicate the azimuthally symmetric large angle sidewards emission of cold ($T < 10$ MeV) matter [Stö80b]. At intermediate impact parameters, a considerable azimuthal asymmetry appears. A strong maximum at small transverse and longitudinal velocities indicates the presence of a large chunk of cold, slowly moving matter, namely the target residue at $\phi = 180°$. A flat local maximum in the projectile hemisphere ($\phi = 0°$) at larger p_{T} and y reflects some sidewards deflected fragments of the beam

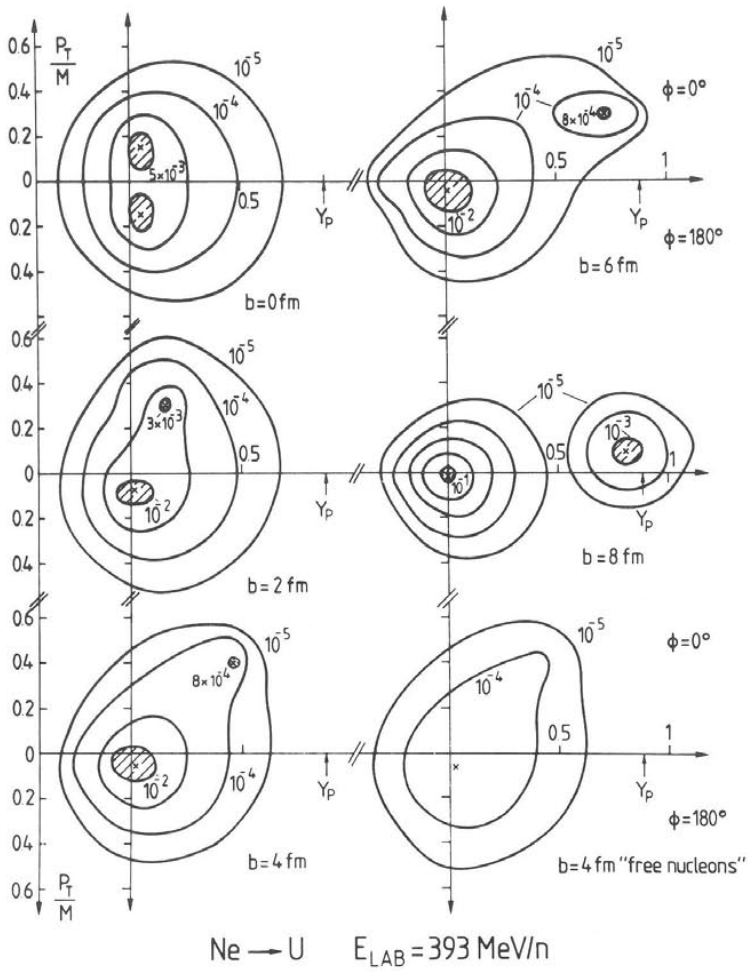

Fig. III.18. The triple differential cross section of emitted nucleons is shown for the reaction Ne (400 MeV/nucleon) + U in the scattering plane as obtained in the fluid dynamical model as a function of impact parameter [Stö82]. A pronounced off-beam axis peak has been predicted as the result of the collective bounce-off effect [Stö80], which has been recently confirmed experimentally [Rit84, Gus84].

particles. The spread of the maxima in ϕ depends strongly on b; for intermediate b it is on the order of $\Delta\phi \sim 40°$. The apparent large collective transverse and longitudinal momentum transfer (the bounce-off process [Stö80b, Mey80, Ren84]) results from the high pressure in the 'participant' head shock zone, pushing the nuclear residues apart to opposite directions ($\Delta\phi = 180°$). This process is of great importance, as it intimately connects the momentum transfer to be observed in bounce-off events with the quantity of central interest, namely, the nuclear equation of state $E(\rho, T)$ [Stö81]. At large impact parameters ($b > 6$ fm) the invariant cross sections peak more closely to the initial projectile and target momenta. Maxima at finite p_T are found even in the azimuthally averaged particle cross sections.

III.3.4. Azimuthal resolution of reaction products

The measurement of the triple differential cross section can yield, however, considerably more information about the collision dynamics: The distance between the jet maxima, i.e., the mean

momentum along the jet axis, may serve as a measure of the transport properties of the matter: For example, a large viscosity slows down the collective fluid motion in the jet direction. There are many other features of the reaction dynamics which are only accessible by detailed inspection of the triple differential cross sections: For head-on collisions of equal nuclei, the compression in the shock zone is maximized, and most of the matter participates in the strong compression. The two-jet patterns give way to an azimuthally symmetric disk of nuclear matter, expanding towards 90° in the c.m. system [Sch74]. It eventually results in doughnut-shaped (toroidal) triple differential cross sections symmetric around the beam axis. The strong collective transverse matter flow [Sch74] with large mean velocity, $p_T/m \approx 0.4$ is caused by the high pressure in the shock region, in analogy to the intermediate impact parameters. Remnants from the squeeze-out can still be seen at small, but finite impact parameters, $b \sim 2$ fm, thus, giving rise to additional out of plane jet structures – four-jet events – at $\theta_{c.m.} = 90°$, $\phi = 90°$, as the outflow of the compressed matter perpendicular to the scattering plane is not hindered by 'spectator' matter. These predictions, however, do not take into account the limitations (e.g., considerable fluctuations) of Eulerian fluid dynamics when applied to light systems: microscopic calculations [Sch81, Ber74, Hal81, Bon76, Ams77, Gud79, Yar79, Cug80, Bod77, Kit78, Bod81] for C + C and Ne + Ne indicate large non-equilibrium contributions. However, while the cascade calculations [Hal81, Yar79, Cug80] – based on free n–n collisions – do not show a considerable transverse momentum transfer even for heavy nuclei, many-body calculations with realistic n–n interactions [Bod77, Kit78, Mol84] predict hydrodynamic features such as the 90° sideways peaking for systems with A_T, $A_P > 40$. We have shown that the experimentally observed cross sections are in good agreement with fluid dynamical calculations. However, triple differential particle cross sections offer a unique tool for the investigation of the complicated reaction dynamics in high energy heavy ion collisions. The combination of the jet analysis with the composition analysis in 4π exclusive experiments, with special emphasis on production and correlations of the different nuclei emitted, can provide snapshots of bulk motion, mass, and temperature distributions, as well as energy and momentum flux in violent nuclear collisions. One problem to be solved in order to obtain triple differential cross section is the necessity to know the experimental reaction plane where $\phi = 0°$, 180°, respectively.

Via the principal axis transformation of the flow tensor discussed below, the azimuthal angle ϕ of the reaction plane may be determined experimentally. Thus, the reaction plane for *each* event is known giving us the opportunity to obtain the *triple* differential cross sections.

III.3.5. 90° out of plane spectra

When a fluid element has been stopped and compressed in the hydrodynamical model calculation, it tries to escape and to expand under a finite angle to the beam axis. In the reaction plane, this angle depends on the impact parameter b. For $b = 0$, the matter flow is perpendicular to the beam axis, for $b = 6$ fm there is a flow angle of $\theta \simeq 10°$.

Perpendicular to the reaction plane, however, there is always a squeeze-out under 90° in the c.m. system (fig. III.19). In that direction the matter can escape freely from the compression zone without being hindered by the target or by projectile mass. Additionally, the cross section of this out of plane matter is not distorted by any spectator material or by corona effects, i.e. it reflects the pure hydrodynamical part of the reaction. The 90° out of plane spectrum is therefore very well suited to study the fluid dynamical behavior of colliding matter. Figure III.20 shows this spectrum for Nb + Nb, 400 MeV/nucleon. In the data of Gutbrod et al. [Gut84] (triangles) high multiplicity events had been selected. The fluid dynamical calculation for $b = 2$ fm reproduces these data very well, as long as an

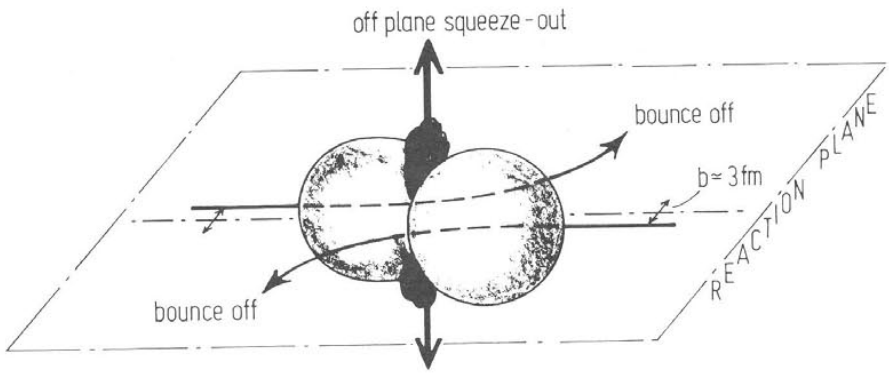

Fig. III.19. Pictorial representation of the in-plane bounce-off and the out of plane squeeze-out of participant matter predicted by fluid dynamics [Stö82, Buc86].

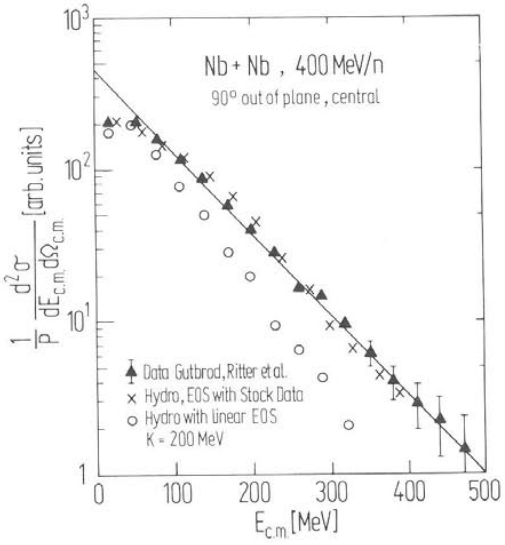

Fig. III.20. Invariant 90° out of plane spectra of protons calculated in the fluid dynamical model [Buc84] with two different equations of state: The soft EOS grossly underpredicts the data, while the stiff EOS agrees well with the recent data of the GSI–LBL Plastic-Ball collaboration [Rit84, Gut84].

equation of state is chosen which fits the pion data of Stock et al. (see section III.2) [Sto82]. The results of this calculation are indicated by crosses. An equation of state having a compressibility of $K = 200$ MeV and an extrapolation being linear in ρ for $\rho \gg \rho_0$ is much too soft (circles) and results in a too 'cold' 90° out of plane spectrum. This soft calculation reflects more or less the data for the lighter Ca + Ca system which indeed is colder [Buc84, 86, Gus84].

As the results seem to depend strongly upon the nuclear equation of state (EOS), the EOS could be determined by taking an excitation function of the high multiplicity selected 90° out of plane temperature which can be directly read from the corresponding spectra. The corresponding experimental analysis is currently under way [Gut84].

III.3.6. Transverse momentum distributions versus rapidity

Once the reaction plane is determined, it is possible to analyze the in-plane and the out of plane momentum components. We will present such an analysis for the fluid dynamical calculation of an Nb + Nb, 400 MeV/N collision.

We will concentrate first on the temporal development of the momentum components perpendicular to the beam axis. Figure III.21 shows the results for p_{perp} in the scattering plane (right column) and out of plane (left column) at $b = 3$ fm (upper line) and $b = 6$ fm (lower line) for various times. In all cases the high momentum tail of the distribution has its largest contribution in the early stage of the compression. Here the highest temperatures appear, leading to a considerable amount of fast particles (full lines). At the end of the compression phase ($t \simeq 25$ fm/c, broken lines) a lot of matter has already started to expand and to cool, reducing the amount of fast particles. This effect continues when the expansion of the system goes on ($t \simeq 34$ fm/c, dots) [Buc84, 86].

It is also very instructive to look at the dependence of the average p_{perp} vector component – projected into the reaction plane – on the rapidity y [Dan85]. Figure III.22 shows the time dependence of this quantity for a $b = 3$ fm collision: the average p_{perp} is driven to higher values during the collision as the flow direction settles at about 30° after the compression phase. The flow tensor therefore is not symmetric to the beam axis (direction of y), thus yielding finite values for the magnitude of $\langle \boldsymbol{p}_{\text{perp}} \rangle$. $|\langle p_{\text{perp}} \rangle|$ increases with increasing y until it reaches a maximum at $|y| \simeq 0.5$.

However, depending on the impact parameter there has to be a maximum of $\langle \boldsymbol{p}_{\text{perp}} \rangle$: At high impact parameters, there is little creation of sidewards flow resulting in $\langle \boldsymbol{p}_{\text{perp}} \rangle_{\max} \simeq 0$. At central collisions, on the other hand, there is azimuthal symmetry in the momentum distribution, and the various $\boldsymbol{p}_{\text{perp}}$ contributions average out to zero. This can be seen in fig. III.23, where in part (a) the $\langle \boldsymbol{p}_{\text{perp}} \rangle (y)$ distribution for $b = 2$, 4 and 6 fm is shown. Here the distribution becomes flatter with *increasing* impact parameter. In part (b) the results for $b = 0$, 1, 2 and 3 fm are shown, and the distribution flattens with

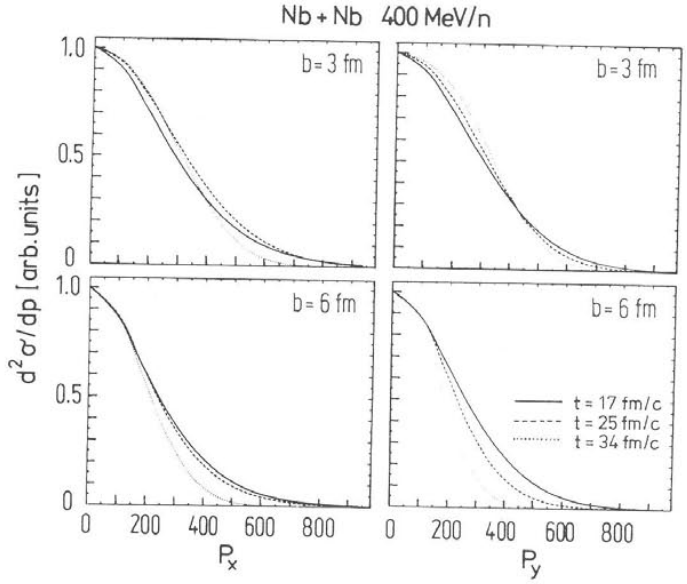

Fig. III.21. The change of the 90° transverse momentum distribution $d\sigma/dp$ with time for the reaction Nb (400 MeV/nucleon) + Nb is shown for various impact parameters [Buc86].

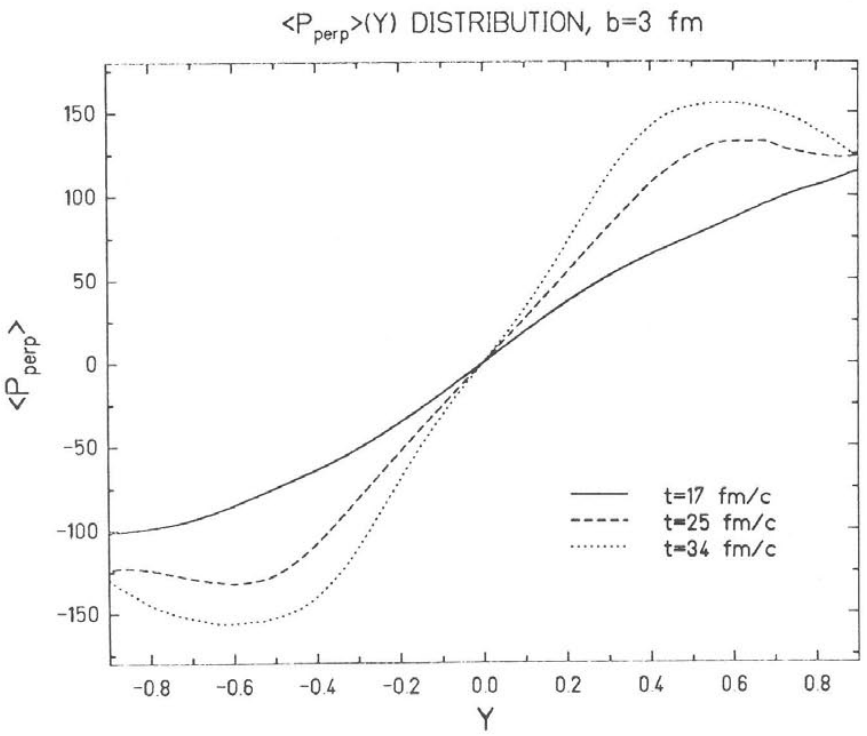

g. III.22. The time dependence of the transverse momentum per nucleon projected in the scattering plane versus rapidity is shown for the system Nb 00 MeV/nucleon) + Nb [Buc86].

ecreasing impact parameter. This effect may offer a unique opportunity to select *very* central events:)ne quantity for that is the charged particle multiplicity $\langle M_c \rangle$, which allows for a selection of $\leq b \leq 3$ fm (see above). When this large $\langle M_c \rangle$ selection is correlated with a low $\langle p_{\mathrm{perp}} \rangle$ trigger, the emaining events must originate from small impact parameter $b \leq 1$ fm. In consequence, these events hould have flow angles in excess of 30°. We will discuss $p_{\mathrm{perp}}(y)$ extensively below.

II.3.7. Macroscopic, fluid dynamical analysis of the kinetic energy flow – Evidence for nuclear stopping nd shock compression

With the cross sections discussed above we have investigated the 'classical' observable of nuclear ollisions. However, this observable describes more or less the *final* state features of the reaction, i.e. he situation after the freeze-out of different matter clusters. Different models like the fireball [Gos78] r the cascade [Yar79, Cug80] reproduce at least some (i.e. inclusive) of the experimental results fairly ell, but one of the important parameters of the different models is always the break-up mechanism hich had been used to obtain the spectra. We have seen above that in this context the fluid dynamical nodel plus chemical equilibrium is a powerful tool to describe the experimental data. However, the rincipal difference between hydrodynamics and other models (i.e. stopping, compression, sidewards emission, bounce-off) cannot be seen in the double differential inclusive spectra. High multiplicity election helps a little, but still more information is needed.

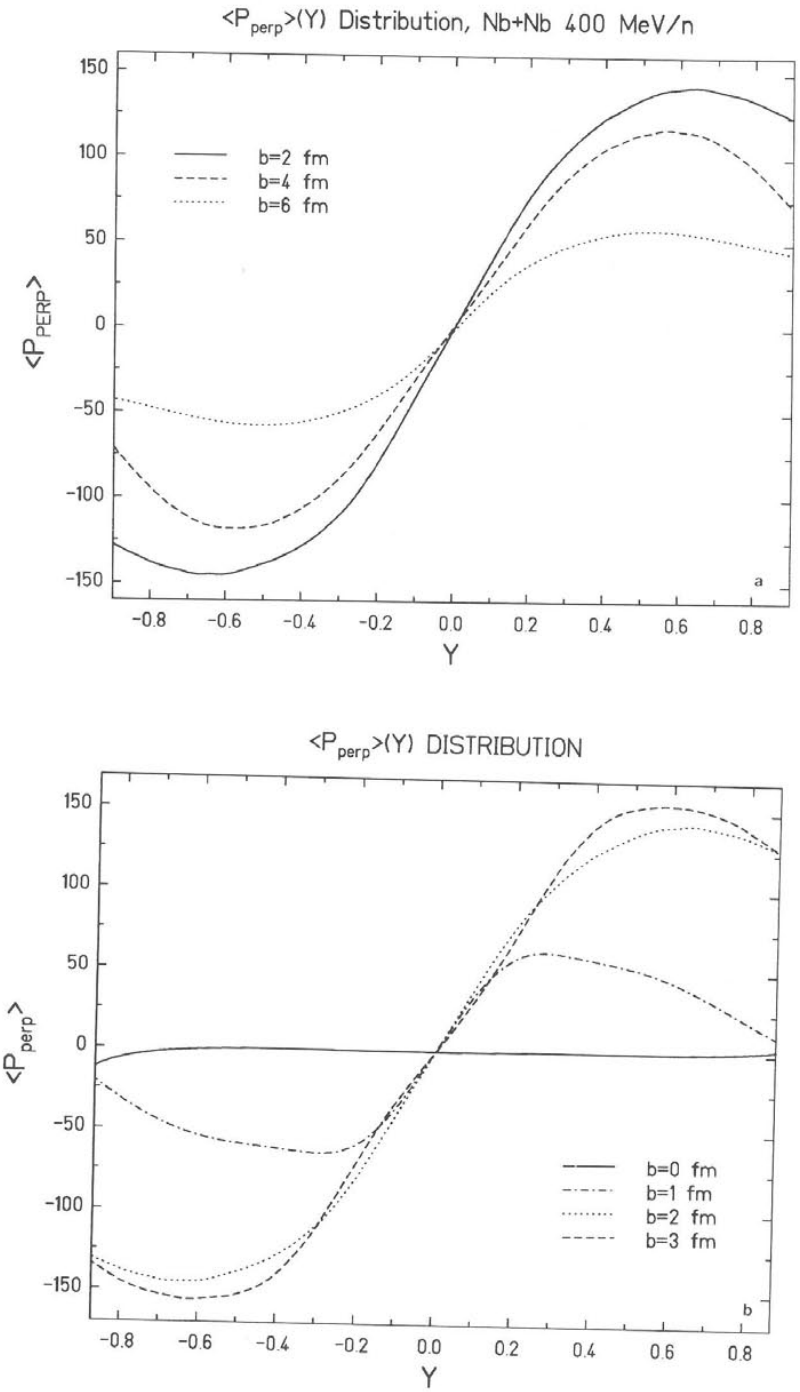

Fig. III.23. The rapidity dependence of the transverse momenta projected into the scattering plane $\langle p_\perp \rangle$ is shown as a function of impact parameter ((a) $b = 2, 4, 6$ fm; (b) $b = 0, 1, 2, 3$ fm) for the system Nb (400 MeV/nucleon) + Nb [Buc86]. Observe that $\langle p_\perp \rangle (y)$ is remarkably similar at $b = 1$ fm and $b = 6$ fm. The maximum $\langle p_\perp \rangle$ is observed at $b = 3$ fm. We would like to point out that for exactly central collisions, $b = 0$ fm, $\langle p_\perp \rangle$ is zero everywhere for symmetry reasons. Therefore one must conclude that the novel transverse momentum analysis proposed by Danielewicz and Odyniec provides valuable information about the momentum transfer only for intermediate impact parameters [Dan85].

It would be very important if we could find more measurable quantities which are influenced in the compression phase only. Then we could decide whether the matter had been stopped and compressed or not. We will discuss such quantities and their interpretation during this section.

The first step in order to find messengers from the compression phase is to look for the quantities which are integrated in the equations of motion.

Such a quantity is the density, for example. However, we have already learned that the density rises and falls off during the reaction, i.e. it has no saturation value. Therefore its asymptotic value cannot carry *detailed* information from the compression phase. A density distribution is not even observable in experiments. The strong sidewards emission of matter observed in figs. III.24–26, on the other hand, should be seen experimentally if matter principally behaves like a fluid.

The same seems to be true for the momentum: the various momentum components have very different histories during the collisions. p_z starts with a high value and is decreased, whereas p_y and p_x are built up. On first glance it again seems that only the direction of $\boldsymbol{p}$ could be an interesting quantity. In the experiment there is only a distinction between $p_\parallel$ and $p_\perp$ possible, reducing the outcome of information. However, we will see later that more detailed information can be obtained by the momentum flow analysis.

As discussed extensively in III.1, another quantity of interest is the entropy. Entropy is generated during the first half of the reaction when the nuclear matter is stopped, compressed and heated. Figure III.2a describes the situation for a Nb + Nb collision at 400 MeV/n and an impact parameter of $b = 3$ fm in detail:

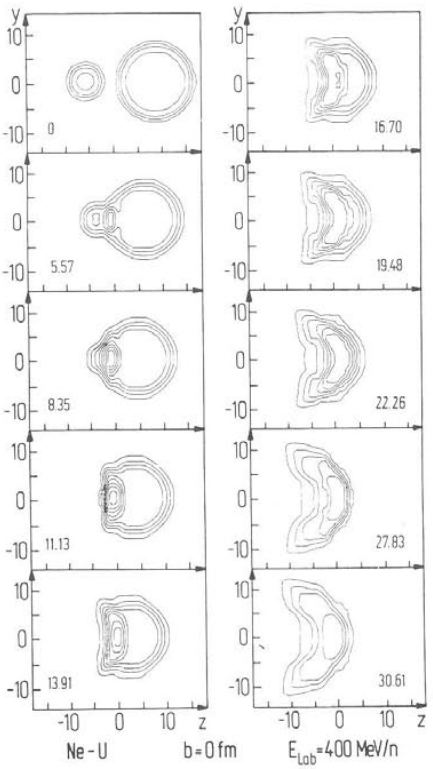

Fig. III.24. Density contour plots as obtained with the non-relativistic nuclear fluid dynamical model [Stö80] for the reaction Ne (400 MeV/nucleon) + U at $b = 0$ fm as a function of time. Observe the directed sidewards flow as a result of the shock wave formation (high density of contour lines).

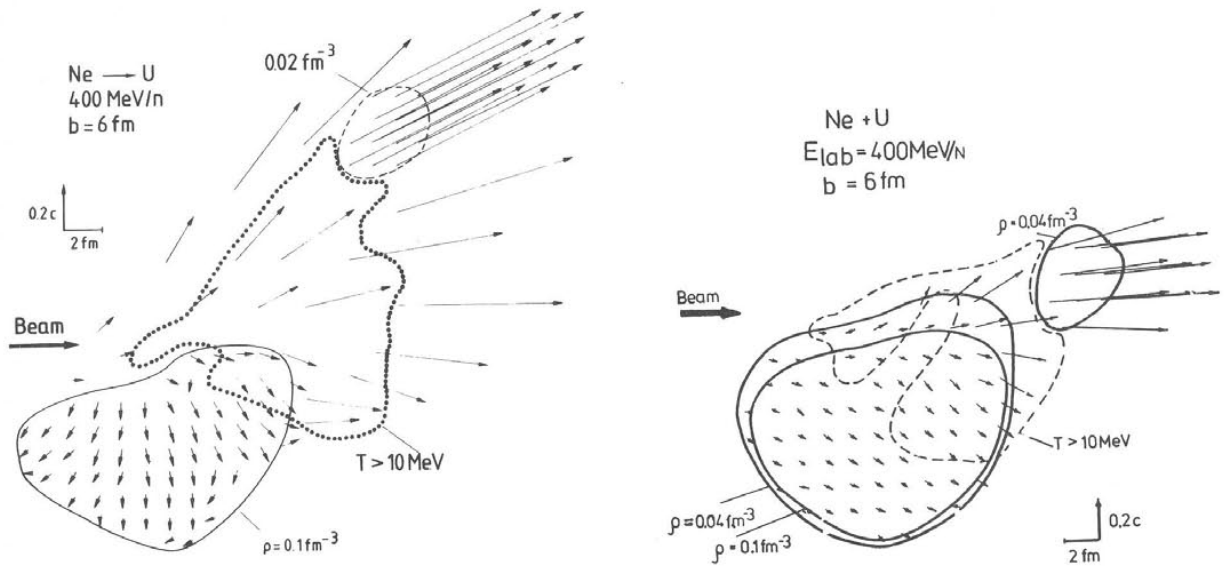

Fig. III.25. Final state of the reaction Ne (400 MeV/nucleon) + U at $b = 6$ fm shown as contour plot in the scattering plane. The recently observed [Rit84, Gus84] strong bounce-off effect predicted by nuclear fluid dynamics (left, [Stö80]) is not reproduced by the microscopic cascade model of Gudima and Toneev (right, [Ton83]), which neglects the repulsive nuclear interactions at high density, i.e. the nuclear compression energy.

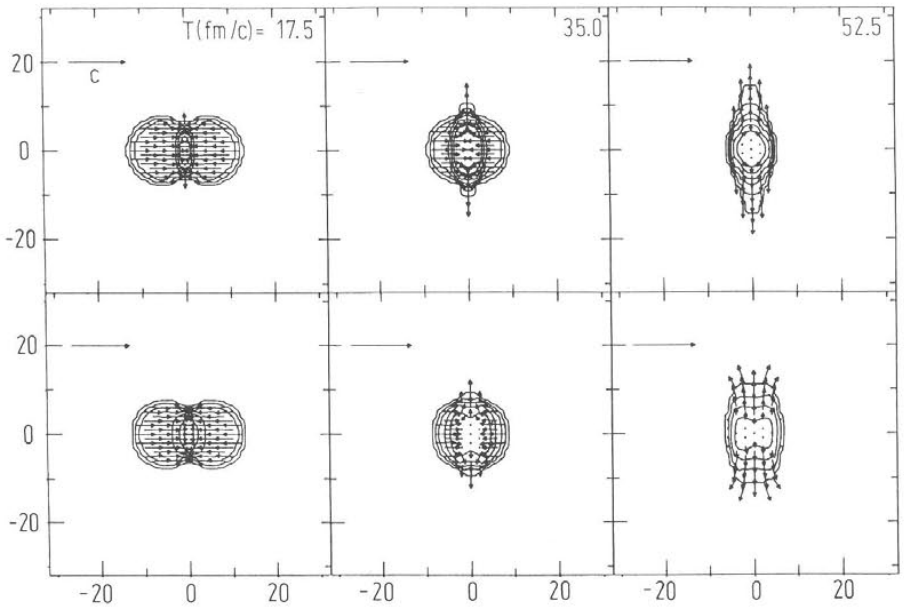

Fig.III.26. Time dependence of baryon density contours [Buc84b, Buc86] for the reaction U (100 MeV/nucleon) + U as calculated by the fluid dynamical model shows clearly the formation of an ellipsoidal compression zone and sideward squeeze-out of matter predicted in earlier schematic approaches of the Frankfurt school [Sch74a, b].

Entropy is created during the first $\simeq 20$ fm/c of the collision (full line). During that time the various zones of the two nuclei are stopped and compressed. When the maximum density of the system starts to drop (broken line after $\simeq 20$ fm/c) the entropy has reached its saturation value of about 2.6. As the subsequent expansion phase is isentropic, this value of S/A is maintained during the rest of the calculation. The entropy even saturates when a large sheer viscosity η is present in the Navier Stokes equations. In fig. III.2(b) it can be seen that for $\eta = 20$ MeV/fm^2c and for $\xi = 20$ MeV/fm^2c the absolute value of the entropy rises from 2.66 (non-viscous) over 2.96 ($\eta = 20$ MeV/fm^2c) to 3.17 ($\xi = 20$ MeV/fm^2c) whereas the asymptotic constancy of these values remains unaltered.

That is due to the fact in the expansion phase no more sheer-flow is present: Either the matter has a collective flow or it expands isotropically. However, the situation changes completely when bulk viscosity ξ is allowed for because then all *expanding* matter is affected. This has not so much influence on the reaction dynamics (see also ref. [Buc81]) but mainly on the expansion phase. There is a substantial entropy production also at late times (fig. III.2b), and a saturation does not occur.

We conclude that entropy is a very interesting quantity, but it is very hard to handle. When bulk viscosity is present, entropy is also generated during the expansion phase of the system and there is little chance of getting 'pure' information from the compression phase only. If there is no bulk viscosity the problem of experimental determination of S/A remains. We have seen above (section III.1) that certain assumptions on the decay of the system are necessary. We will therefore concentrate on other interesting quantities.

Figure III.27 shows the average values of total (full line), cold internal (point-dotted), kinetic (dotted) and thermal (broken) energy obtained during a fluid dynamical simulation of a central Nb + Nb collision at 400 MeV/n in the c.m. system. In principle, the total energy contained in the system should stay

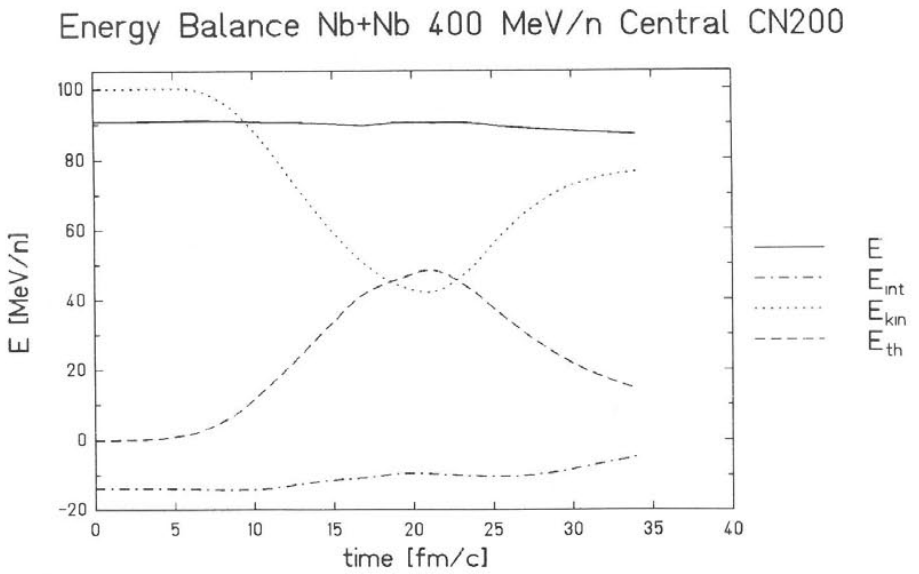

Fig. III.27. Division of the total energy into various channels as a function of time in the reaction Nb (400 MeV/nucleon) + Nb. The fluid dynamical model predicts that with the soft equation of state, the transformation of the incident kinetic energy proceeds predominantly into random thermal motion E_{th}. Observe that substantial collective macroscopic motion is present at all times; total collective stopping of all regions of the projectile and target at the same instant of time does not occur. This is due to the beginning of the collective sidewards expansion, which yields transformation of random microscopic motion into collective flow, before all parts of the initial nuclei have participated in the reaction [Buc86].

constant. The small energy loss (about 1% of the lab energy) in fig. III.27 is due to numerical reasons and will be neglected in the further discussion.

When the two nuclei touch each other after about 5 fm/c the matter in the contact zone is stopped, thus reducing the average kinetic energy in the whole system. Due to the supersonic incident velocity a shock front is created resulting in heat production. As the matter is compressed, the cold internal energy smoothly raises from its minimum at $W_0 = -16$ MeV to larger values. During the next $\simeq$15 fm/c, more and more matter undergoes the process described above. However, the matter which had been stopped first, already starts to expand again (see e.g. fig. III.28). Therefore the *mean* kinetic energy does not reach zero, i.e. the system is never stopped in total. The expanding matter cools, resulting in a drop of the mean thermal energy. However, the cold internal energy still rises because the density now drops below the equilibrium value of $\rho_0 = 0.17\,\mathrm{fm}^{-3}$.

Finally, after roughly 30 fm/c, the mean kinetic energy of the expanding system seems to saturate at about 80 MeV/n in the c.m. system. Obviously, $E_{\mathrm{kin}} = p^2/2m$ is a quantity saturating once the compression phase is over. However, the scalar E_{kin} contains only limited information. It would be important to know, if more general quantities as, for example, quadratic combinations of the momentum components $p_i p_j$ have these saturation features too. The idea and the results of such a 'global momentum tensor analysis' (flow analysis) will be discussed in this paragraph.

The collective flow, predicted by fluid dynamical calculations [Stö 79–84, Buc 80–84] could be observed directly by the global momentum tensor analysis: This analysis can be done experimentally with 4π detector systems such as emulsion, streamer chamber, or the plastic ball. The basic idea is to measure event by event the momenta of all (charged) particles. Once this information is available, one can transform all the physical quantities into the center of momentum frame and determine the

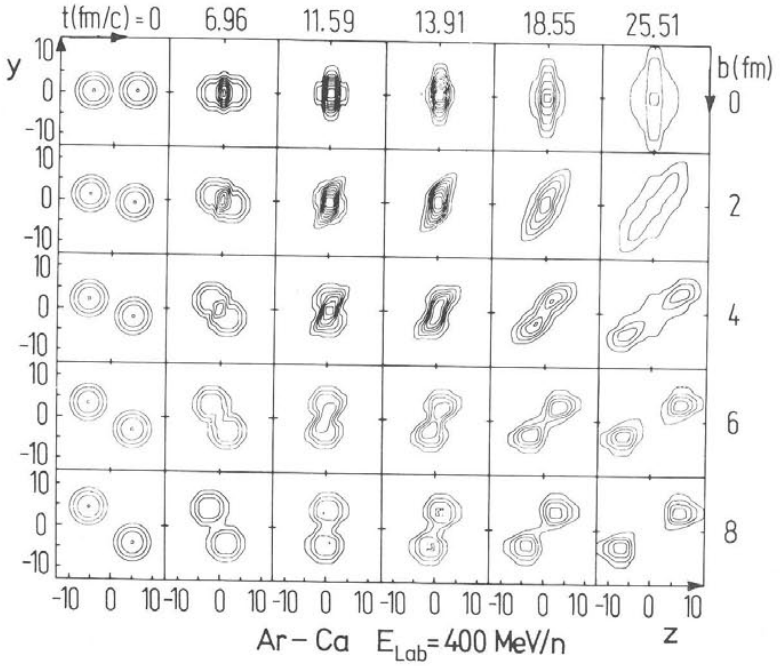

Fig. III.28. The fluid dynamical predictions for the impact parameter dependence of the baryon density contours as a function of time for the system Ar (400 MeV/nucleon) + Ca [Stö80]. Observe the transition from the bounce-off dominated intermediate impact parameters to the 90° squeeze-out at $b = 0$ fm.

direction of maximum momentum and energy flow by performing a principal axis transformation. The various concepts which have been proposed to analyze nuclear collisions are thrust [Kap81, Cug82], sphericity [Cug82, Gyu82, Stö82], kinetic energy flow [Gyu82, Stö82, Buc83d]. The first two concepts have been adapted from high energy physics, but they have the disadvantage of being either non-analytic (thrust) or of not properly taking into account the emission of composite particles (sphericity). The kinetic energy flow tensor [Gyu82, Stö82, Buc84d],

$$F_{ij} = \sum \frac{p_i(\nu)\, p_j(\nu)}{2m_\nu}, \tag{III.18}$$

where the sum runs over all fragments ν with mass and center of mass momentum $\boldsymbol{p}(\nu)$, is a generalization of the sphericity concept. The factor $(2m_\nu)^{-1}$ ensures that composite fragments contribute to the matter flow tensor with the correct weight relative to nucleons.

By comparing the results of the cascade and the hydrodynamic calculation, we want to determine the sensitivity of the global variables to the collision dynamics. In cascade calculations, $m_\nu = m_N$ and the $\boldsymbol{p}(\nu)$ are the final momenta of all nucleons. In hydrodynamic calculations the reaction volume is divided into cells ν characterized by a mean flow velocity, $\boldsymbol{p}(\nu)/m_N$, a local temperature $T(\nu)$, and a local baryon number $N(\nu)$. The baryon density in a cell contributes an amount $\bar{p}_i\bar{p}_j/2m + \delta_{ij}T/2$ to the flow tensor. Thus, for hydrodynamics F_{ij} is the sum of a collective flow energy $\bar{F}_{ij}$ and a thermal energy $\delta_{ij}E_T/3$,

$$F_{ij} = \sum_\nu \frac{\bar{p}_i(\nu)\, \bar{p}_j(\nu)}{2m_N} + \delta_{ij}\, \tfrac{1}{2}T(\nu) = \bar{F}_{ij} + \delta_{ij}E_T/3\,. \tag{III.19}$$

Observe that the eigenvalues of F are then $\lambda_n = \bar{\lambda}_n + E_T/3$, where $\bar{\lambda}_n$ are the eigenvalues of $\bar{F}$. However, the eigenvectors, $\hat{e}_n$, are identical to those of F. Thus, while the aspect ratio, $R_{13} = \lambda_1/\lambda_3$ $(\lambda_1 > \lambda_2 > \lambda_3)$ is brought closer to unity by thermal smearing, the flow angle $\theta_F = \cos^{-1}(\hat{e}_1 \cdot \hat{z})$ is unaffected by temperature. Experimentally, this procedure can always be done, and there will be a distinguished average value for R_{13} and θ_F. In the fluid dynamical model, there is a saturation for R_{13} and θ_F once the compression phase is over. This value then is conserved to the asymptotic times. Figure III.29 shows the temporal development of R_{13} and θ_F for a central Nb(400 MeV/n) + Nb collision [Buc84, 86]. First, when the two nuclei approach each other, we have a very stretched tensor. Subsequently the matter is stopped and the flow ratio is reduced (nearly to 12 to 18 fm/c). During that time the main flow proceeds parallel to the beam axis, i.e. θ_F is zero. After $\simeq$18 fm/c the expansion of the system is the dominating component of the kinetic flow. The main contribution now stems from matter flowing perpendicular to the beam axis. As the λ_i are ordered by magnitude, there is a sudden flip in the flow angle θ_F from 0° to 90° when the $p_\perp$ contribution starts to be larger than $p_\parallel$. After about 23 fm/c, i.e. when the compression phase is just over (see contour plot in fig. III.30), the flow ratio R_{13} saturates at $R_{13} \simeq 2$. This is much earlier than the saturation of E_{kin} in fig. III.27.

In fig. III.31 we plot the flow angle $\theta_{flow}^{c.m.}$, i.e., the angle of the largest principle axis of the flow tensor to the beam axis, versus the aspect ratio R_{13} for the reaction U(400 MeV/nucleon) + U [Buc 83a, b]. Note that $R_{13} \gg 1$ reflects events stretched in momentum space, while $R_{13} = 1$ indicates a spherical momentum distribution. The ridge in the (θ_{flow}, R_{13}) plane resulting from the cascade calculations depends on the total mass of the systems. The cascade calculations [Cug82, Gyu82] show that substantial flow angles should only be expected for very heavy systems $A_1 = A_2 > 100$.

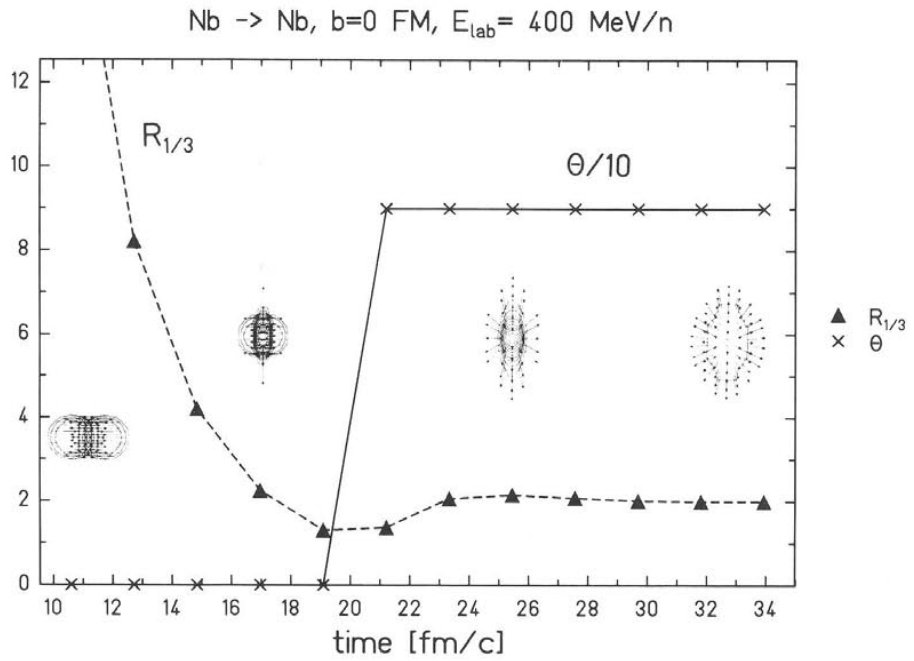

Fig. III.29. Time dependence of the aspect ratio R_{13} and the flow angle θ_F as obtained from the fluid dynamical calculation for the reaction Nb (400 MeV/nucleon) + Nb at $b = 0$ fm. We would like to point out that both R_{13} and θ saturate at the point of highest density and are conserved during the expansion. Therefore, both R_{13} and θ can serve as messengers for the high density stage of the reaction [Buc84, 86].

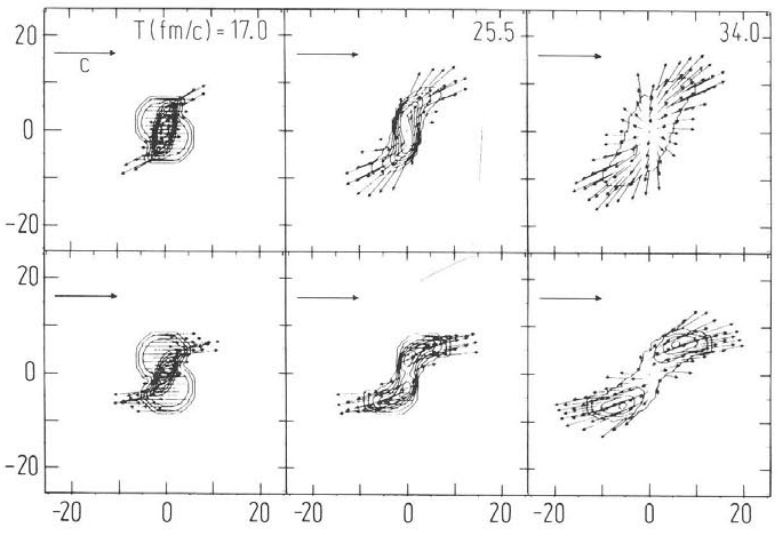

Fig. III.30. The change of the flow angle with impact parameter (upper row: $b = 3$ fm, lower row: $b = 6$ fm) becomes obvious in these density contour plots for the system Nb (400 MeV/nucleon) + Nb obtained with the fluid dynamical model [Buc84].

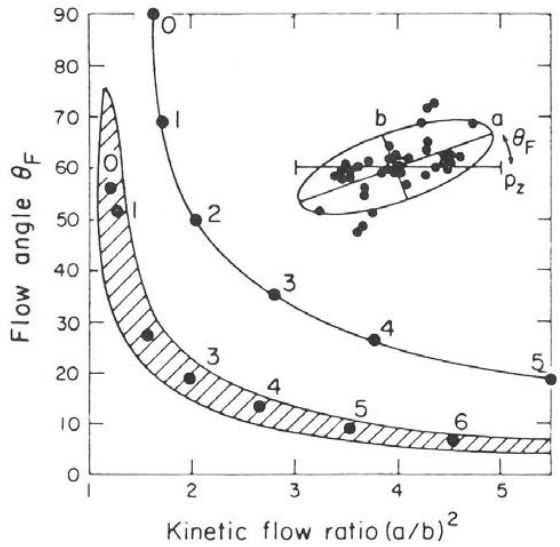

Fig. III.31. Kinetic energy flow analysis for U(400 MeV/nucleon) + U is shown in the R_{13}–θ plane for the cascade model calculation (the shaded area) and the fluid dynamical calculation (solid line). The numbers indicate the impact parameter in fm [Buc83].

Furthermore, there are substantial finite number distortions [Dan84] of the flow characteristics for $A < 100$. Also shown are the results of the fluid dynamical calculation for the same system. Larger deflection angles and aspect ratios R_{13} indicate that the matter flux is apparently more strongly correlated for the hydrodynamical model. The impact parameter dependence of the flow angle, θ_F, aspect ratio R_{13}, sphericity $S = \frac{3}{2}(\lambda_1 + \lambda_2)$, and coplanarity (or flatness) $C = \frac{3}{2}(\lambda_2 - \lambda_1)$ with $\lambda_1 < \lambda_2 < \lambda_3$ the principal values [normalized by $(\mathrm{Tr}F_{ij})^{-1}$] is shown in fig. III.32 for the hydrodynamic model

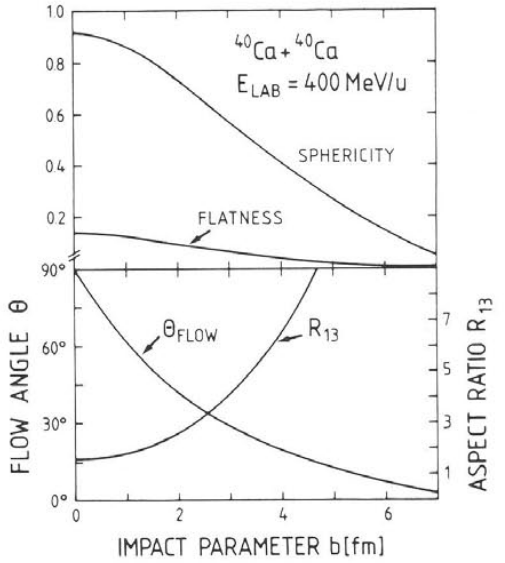

Fig. III.32. The impact parameter dependence of R_{13}, θ_{flow}, sphericity, and coplanarity is shown as calculated for the reaction ^{40}Ca (400 MeV/nucleon) + ^{40}Ca in the fluid dynamical model [Stö82].

calculation for the system ^{40}Ca(400 MeV/nucleon) + ^{40}Ca. Observe the greater sensitivity of θ_F, R_{13} to impact parameter than that of S and C. Also note that $R_{13} = 1.7$ at $b = 0$ is remarkably close to the value computed via cascade for this reaction in [Gyu82]. However, this coincidence is due only to finite number distortion effects in cascade calculations. As shown in [Dan84], a sphere sampled randomly by M particles results in $R_{13} \approx 1 + 3/\sqrt{M} + 22/M \approx 1.6$ for $M = 80$. In hydrodynamics, the limit $M \to \infty$ is taken. Therefore $R_{13} = 1.7$ in hydrodynamics represents true collective flow, while in cascade this value is consistent with an isotropic sphere sampled by 80 particles.

The general behavior of the flow pattern in the fluid dynamical model is as follows: The flow angle rises smoothly from 0° at large impact parameters to 90° at $b = 0$, while sphericity and coplanarity rise from 0 to 0.9 and 0.2, respectively. Since the matter flow reflects the longitudinal, $p_\parallel$, and transverse $p_\perp$, momentum transfer in a collision, it can be used to directly measure the pressure built up in the high density stage of the reaction [Stö81d]

$$p_\perp = \int_t \int_f P(\rho, S)\, \mathrm{d}f\, \mathrm{d}t\,, \tag{III.20}$$

where $\mathrm{d}f$ represents a surface element between the participant and the spectator matters and the total pressure $P(\rho, S)$ is the sum of an interaction pressure $P_C(\rho, S = 0)$ and a kinetic term $P_T(\rho, S = 0)$

$$P(\rho, S) = P_C(\rho, S = 0) + P_T(\rho, S > 0)\,. \tag{III.21}$$

The bombarding energy dependence of $(P_C + P_T)/P_T$, i.e., the ratio of the total pressure to the Fermi-gas term, has been calculated in [Stö81a] see fig. III.33a. The results show that there is a strong bombarding energy dependence of $P/P_T(E_{Lab})$. The kinetic term P_T dominates at high energies, $E_{Lab} >$ MeV/nucleon, while the interaction term P_C far exceeds P_T at intermediate energies,

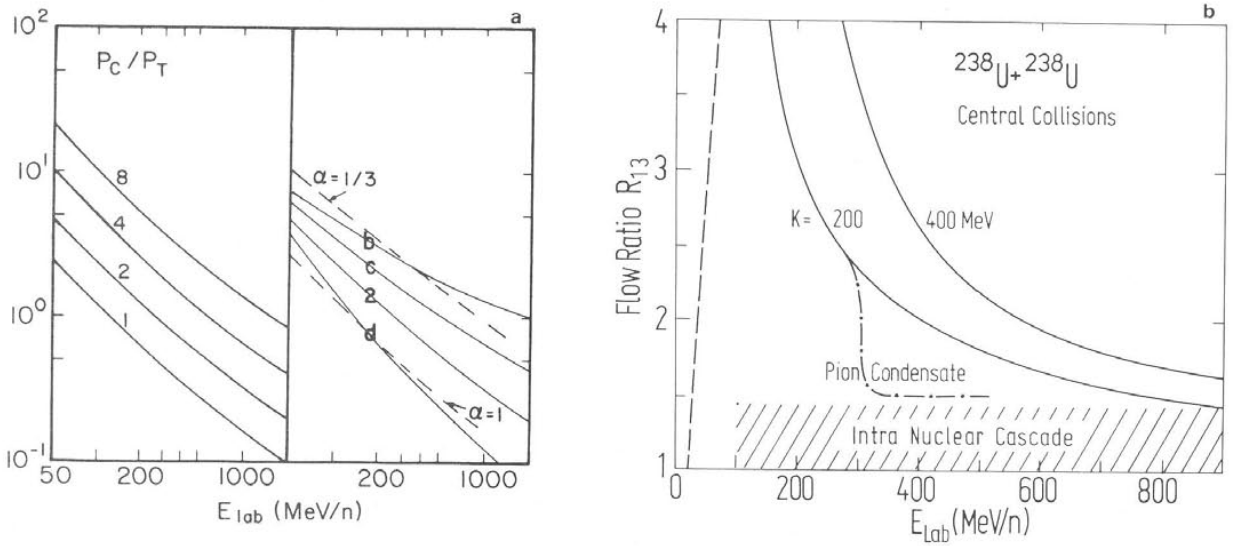

Fig. III.33. The bombarding energy dependence of (a) the ratio of compression-to-thermal pressure for various compression constants [Stö81] and (b) the aspect ratio R_{13} is shown for central collisions of uranium on uranium. The dashed area in (b) indicates the results of the cascade calculation; the solid lines in (b) represent the results of the fluid dynamical model for different equations of state [Buc83].

≤ 200 MeV/nucleon. Second, the total pressure is most sensitive to the stiffness of the nuclear equation of state at energies ≤ 200 MeV/nucleon. Since the flow characteristics depend directly on the pressure, we can expect a dependence of the flow pattern on the stiffness of the equation of state. To check this idea we have investigated in fig. III.33b the bombarding energy dependence of the kinetic flow ratio R_{13} for central collisions of U + U using both the fluid and cascade model [Buc83a, b].

Figure III.33b shows an important result: We find a strong energy dependence of $R_{13}(E_{\mathrm{Lab}})$ in the fluid dynamical calculation, which indeed closely reflects the energy dependence of $P/P_{\mathrm{T}}(E_{\mathrm{Lab}})$ discussed above. This is in strong contrast to the cascade results (shaded area in fig. III.33b) that show no appreciable indications for a dependence of R_{13} on the bombarding energy, even for the heavy system U + U. The values $R_{13}^{\mathrm{cascade}} \leq 1.5$ reflect only a globally thermalized "fireball" momentum distribution. In particular, finite number effects [Dan84] map $R_{13} = 1.0$ into $R_{13} \sim 1.2$ for $M = 476$. The strong collective flow, as observed in the hydrodynamical calculations is not seen. At high energies, $E_{\mathrm{Lab}} > 1$ GeV, both approaches yield similar values $R_{13} < 1.5$. In hydrodynamics R_{13} approaches unity because the isotropic thermal flow $\delta_{ij} E_{\mathrm{T}}/3$ dominates the directed collective flow $\bar{F}_{ij}$ in eq. (III.19) at high energies.

Again, for finite impact parameters, there is the same behavior. The curves are only shifted by a constant. The dependence of $R_{13}(E_{\mathrm{Lab}})$ on the nuclear compressibility is of particular interest. Figure III.33b shows $R_{13}(E_{\mathrm{Lab}})$ for three different equations of state. As with the dependence of P/P_{T} on the compressibility, R_{13} increases (at a given bombarding energy) if the compressibility [and hence $P_{\mathrm{C}}(\rho)$] is increased. This finding shows that global event analysis as a function of beam energy can indeed provide information on the stiffness of the equation of state. The measurement of $R_{13}(E_{\mathrm{Lab}})$ can also allow for an experimental search for abnormal superdense states (pion condensates, density isomers, in general bends and secondary minima in the interaction pressure), which would reveal themselves by a threshold decrease of R_{13} at the critical bombarding energy $E_{\mathrm{Lab}}^{\mathrm{crit}}$ sufficient for a transition into an abnormal state to occur. The decrease of the interaction pressure P_{C} may even lead to metastable density isomeric states. Just above the barrier to such a hypothetical abnormal state, P_{C} would be negative and inhibit an immediate decay of this state [Stö79]. The consideration of such abnormal states is speculative. However, our point is that $R_{13}(E_{\mathrm{Lab}})$ is a sensitive probe to exotic phenomena as well.

To compare with actual experiments, the ideal hydrodynamic model predictions will have to be corrected for the contribution to F due to nucleons that suffer too few collisions to evolve hydrodynamically. First, there are spectator nucleons that do not suffer any large momentum transfer collisions in the first place. Second, there are knock-out nucleons which suffer only one NN collision. Finally, there are intermediate collision nucleons that suffer 2–3 collisions. These nucleons will be distributed approximately isotropically in the c.m. frame [Sch81].

To incorporate such non-hydrodynamical background, we decompose F according to the number of collisions made by nucleons [Buc83a, b]

$$F = \sum_{n=0}^{\infty} P(n)\, F(n)\,, \tag{III.22}$$

where $P(n)$, with $\Sigma P(n) = 1$, is the relative weight of the contribution of nucleons, which collided n times, to F, and $F(n)$ is the flow tensor associated with the final distribution of such n collision nucleons in momentum space. We normalize F to unit trace in eq. (III.22) by requiring $\mathrm{Tr}\, F(n) = 1$ for all n. At best, the flow tensor calculated in hydrodynamics can approximate $F(n)$ for $n \gg 1$. To gain insight into the effect of small n contributions, we divide eq. (III.22) into three main terms,

$$F = p_0 F_0 + p_1 F_1 + (1 - p_0 - p_1)\bar{F}, \tag{III.23}$$

where $\bar{F}$ is given by eq. (III.19), $p_0 = P(0) + P(1)$ is the weight of spectator and direct knockout nucleons, and p_1 is the fraction of nucleons suffering an intermediate number of collisions with $N_c \sim 2$–3. The spectator plus knock-out contribution F_0 is approximated by

$$F_0 = \mathrm{diag}(0, 0, 1), \tag{III.24}$$

since the spectator nucleons and – due to the forward–backward peaking of the N–N cross section – also the knock-out nucleons are concentrated around ± the incident c.m. momentum per nucleon. For simplicity, we approximate the intermediate collision contribution, $N_c = 2$–3, by an isotropic momentum distribution for which

$$F_1 = \mathrm{diag}(\tfrac{1}{3}, \tfrac{1}{3}, \tfrac{1}{3}). \tag{III.25}$$

Finally, for central collisions, for which $\bar{F}$ in eq. (III.19) is diagonal,

$$\bar{F} = \frac{1}{2 - r_h}\,\mathrm{diag}(1, 1, r_h) \tag{III.26}$$

the full tensor has the diagonal form

$$F = \frac{1}{2 + r}\,\mathrm{diag}(1, 1, r). \tag{III.27}$$

Note, for example, from fig. III.33 that $r_h \sim 0.5$ for the U + U collision at 400 MeV/nucleon. For $0 < r < 1$, F in eq. (III.27) describes a pancake shape with aspect ratio $R_{13} = 1/r$ and flow angle $\theta_F = 90°$. For $r > 1$, F describes a cigar shape with $R_{13} = r$ and $\theta_F = 0°$.

The effect of adding F_0 and F_1 to F in eq. (III.23) is to replace the hydrodynamic value, r_h, by r given by [Buc83a, b]

$$r/(r + 2) = p_0 + p_1 + (1 - p_1) r_h/(2 + r_h). \tag{III.28}$$

For example, for $r_h = \frac{1}{2}$, i.e., $R_{13} = 2$, the measured r exceeds 1 if the fraction of spectator nucleons p_0 exceeds $\frac{1}{6}$. With $p_1 = \frac{1}{4}$, $r > 1$ when $p_0 > \frac{1}{8}$.

Equation (III.28) shows that the magnitude of R_{13} in fig. III.33b can be significantly reduced as a result of the non-hydrodynamic background contributions. Only a 5% spectator contribution is required to lower R_{13} from 4 at 300 MeV/nucleon in fig. III.33b to 2.7. Alternately, a 25% intermediate isotropic background is sufficient to reduce R_{13} to 2.5 from 4. Therefore, in comparing data to the hydrodynamic predictions in fig. III.33b, the substantial modification of R_{13} due to the background must be taken into account. The presence of the nucleons with $N_c \leq 3$ also means that the hydrodynamic calculation should only be started after the few collision initial stage with densities depleted to the value $\rho_0(1 - p_0 - p_1)$ instead of using all the nucleons. However, due to the scaling of the hydrodynamic equations with the nucleon number A (i.e., since the results of the calculations are practically independent of A), we do not anticipate a qualitative change of the hydrodynamic results.

A simple way to eliminate the spectator and knock-out contributions is to remove nucleons with momenta in a shell of radius $p_{c.m.}$ and thickness $\Delta \sim 100\,\mathrm{MeV}/c$ from the sum of eq. (III.23). However, it is not so simple to remove the approximate isotropic background F_1. One possibility is to estimate that component via an intranuclear cascade calculation.

We will now report a detailed analysis of the reaction Nb(400 MeV/N) + Nb based on nuclear fluid dynamics and intranuclear cascade simulations. The theory is compared to recent experimental data of Ritter et al. [Rit84], who studied this system with the 'Plastic Ball' 4π electronic detector system.

The general behavior of the flow pattern in the fluid dynamical model is recapitulated as follows: The flow angle θ_f rises smoothly from 0° at large impact parameters to 90° at $b = 0$. Since the contribution of zero impact parameters to the actual experiment is negligible, the theory has to sample over a range of finite impact parameters before it can be compared to the data.

The major cause of concern for a direct comparison of the data to the hydrodynamical predictions is, however, the finite multiplicity, $M < 50$, of emitted fragments: There are substantial finite number distortions [Dan84] to the kinetic-energy-flow analysis for multiplicities $M < 100$. Therefore, a direct comparison of the conventional 'infinite-particle-number' hydrodynamics with the "raw" finite multiplicity experimental data is inhibited. Only for very massive systems such as uranium on uranium could the finite-particle-number distortions be considered reasonably small. There are two ways out of this dilemma: The first is to correct for the finite multiplicity distortions in the experimental data via an unfolding procedure, which extrapolates the data to the thermodynamic limit, i.e., towards infinite particle number. The second method, applied in this work, incorporates the finite multiplicity effects via a Monte Carlo procedure into the theory. This is done by random sampling of a given fragment multiplicity from the momentum-space distribution of the flow tensor as obtained from the fluid dynamical calculation. This procedure has the distinct advantage that the detector efficiencies can be folded into the theoretical analysis, thus allowing for an unbiased, direct comparison of theory and data. In particular, the restriction to light fragments $Z \leq 2$, the low-energy cutoff ($E^{\mathrm{cut}}/A < 25$ MeV), and the backward-angle acceptance hole of the Plastic Ball ($\theta_{\mathrm{lab}}^{\mathrm{cut}} > 160°$) have been taken into account in the present analysis [Buc84].

Figure III.34 shows the distribution of flow angles, $\mathrm{d}N/\mathrm{d}\cos\theta_{\mathrm{F}}$, thus obtained in comparison with the experimental data and the intranuclear cascade calculation [Gus84, Yar79]. The fragment yield calculation performed after the break-up of the fluid yields average multiplicities from $M = 35$ at $b = 6$ fm to $M = 46$ at $b = 0$. The dispersion of multiplicities around these values has not been taken into account. The theoretically obtained high-multiplicity triggered events, corresponding to the small impact parameters ($b = 0$ to 3 fm), compare favorably with the high-multiplicity selected experimental data. Both exhibit average sidewards flow angles of $\theta_{\mathrm{F}} = 30°$, whereas the high-multiplicity selected events of the cascade calculation [Gus84, Yar79] exhibit strongly forward-peaked distributions. This observation of collective sidewards flow represents the first unambiguous evidence for the formation of high density matter, which has been predicted on the basis of nuclear fluid dynamics a decade ago [Sch74]. Thus the key mechanism for the investigation of the nuclear equation of state has been experimentally established. It is surprising that the predicted 90° flow [Sch74, Hof76, Stö78] can be observed neither in the data nor in the fluid calculation. This is due to the rapid falloff of θ_{F} for $b > 0$: $\mathrm{d}N/\mathrm{d}\cos\theta$ is dominated by contributions from $b = 2$–3 fm. Only for much heavier systems, e.g., U + U, would this range of b values reveal flow angles $\theta_{\mathrm{F}} \gtrsim 60°$. The intermediate multiplicities ($30 < M < 40$) correspond to larger impact parameters, $b < 6$ fm in the hydrodynamical plus statistical break-up calculation. The experimentally observed decrease of the average flow angle ($\theta_{\mathrm{F}} = 15°$) is well reproduced by the fluid dynamical calculation. The lowest interval of multiplicities, $M < 20$, corresponds to large impact parameters, where the projectile and target remnants cause the strong 0° peak in $\mathrm{d}N/\mathrm{d}\cos\theta_{\mathrm{F}}$.

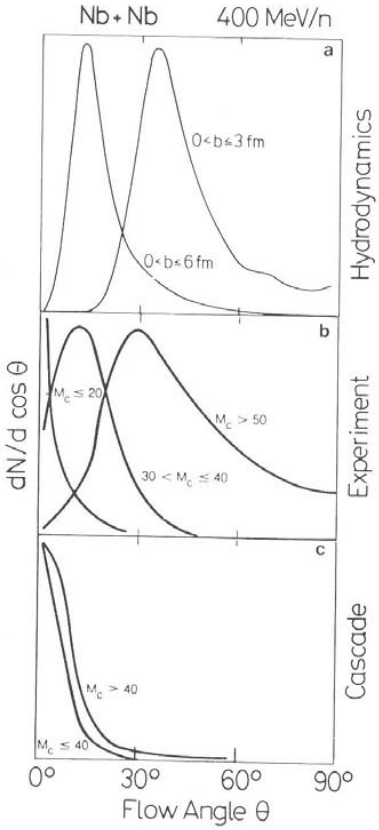

Fig. III.34. Distributions of flow angles $dN/\cos\theta_f$ for the reaction ^{93}Nb(400 A MeV) + ^{93}Nb. (a) Result for the hydrodynamical calculation [Buc84a]. The finite-multiplicity distortions are taken into account. The given impact-parameter ranges correspond to the multiplicity cuts indicated at the experimental curves below [(b)]. (b) Plastic Ball data [Rit84, Gus84] for various multiplicity cuts given at the curves. (c) Result of the cascade simulation after multiplicity selection [Gus84].

Let us now consider the asymmetric system Ar + Pb at 800 MeV/N, which is the heaviest system to date for which 4π data exist at relativistic energies. Also the streamer chamber measurements by the GSI–LBL–Heidelberg collaboration [Str83] indicate consistently larger flow angles and more isotropic aspect ratios than are predicted by the cascade code of Cugnon et al. [Cug82]. This may be taken as further evidence for a fluid dynamical behavior of this system. The details of the analysis, however, make a quantitative comparison with fluid dynamical calculations difficult, as discussed below.

We present the results of a 3-dimensional relativistic fluid dynamical calculation for Ar + Pb coupled with a generalized flow analysis using relativistic kinematics [Gra84]. The center of momentum frame used to construct the flow tensor,

$$F_{ij} = \sum_{\nu} w(\nu)\, p_i(\nu)\, p_j(\nu) \tag{III.29}$$

is determined by the 'participants', defined in the experiment [Str83] as all particles with transverse momentum $p_t > 270$ MeV/c. In contrast to a symmetric system, the velocity of this participant CM is not constant, but ranges from the compound nucleus limit for central collisions to the nucleon–nucleon limit (and beyond) for peripheral collisions (fig. III.35).

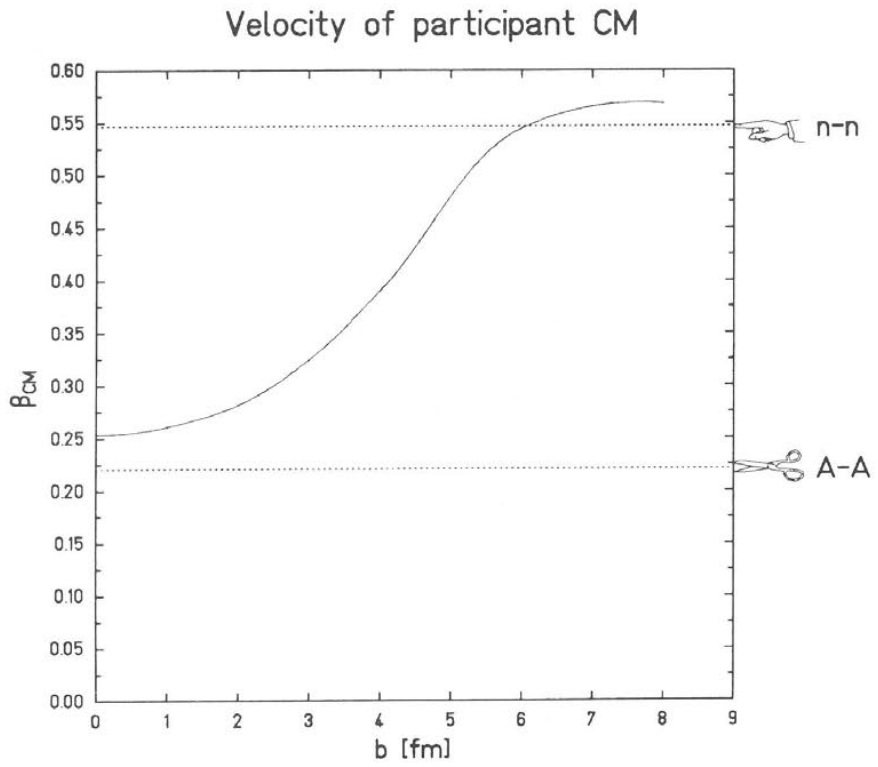

Fig. III.35. The impact parameter dependence of the velocity of the participant center of mass system as calculated in the relativistic fluid dynamical model for the reaction Ar (0.8 GeV/nucleon) + Pb [Gra84].

The experimental analysis is restricted to charged particles in the forward hemisphere of the participant CM. The transverse energy E_t of these particles, defined as

$$E_t = \sum_\nu \{[p_t(\nu)^2 + m(\nu)^2]^{1/2} - m(\nu)\} \tag{III.30}$$

is found to decrease with increasing impact parameter b in the cascade and hydrodynamical models and is used experimentally as a measure for b. The flow tensor F_{ij} is diagonalized with the weight function $w(\nu) = 1/|p(\nu)|$. This has properties similar to the kinetic flow tensor (eq. (III.19)), with $w(\nu) = 1/2m_\nu$, but does not show collective effects as clearly. This is seen in fig. III.36 which shows the aspect ratio R_{12} (largest eigenvalue of F_{ij} to second) as a function of E_t for the weights

$$w(\nu) = 1/(2m(\nu)),\ 1/(|p(\nu)|),\ 1/(|p(\nu)|)^2\,. \tag{III.31}$$

The choice of R_{12} and the $1/|p|$ weighting, instead of R_{13} and $1/2m$ as in the other analyses presented here, has been introduced by the experimentalists to facilitate the analysis of the streamer chamber data. We would like to point out that $R_{12} \to 1$, does not necessarily imply isotropy but would also emerge from oblate shapes of F_{ij}. The flow angle θ_F is essentially independent of $w(\nu)$ but R_{12} and hence the sensitivity of the flow analysis to dynamical effects decreases for increasing powers of $1/|p|$ and tends towards a constant value of 1 independent of E_t. Figures III.37 and III.38 show the R_{12} and

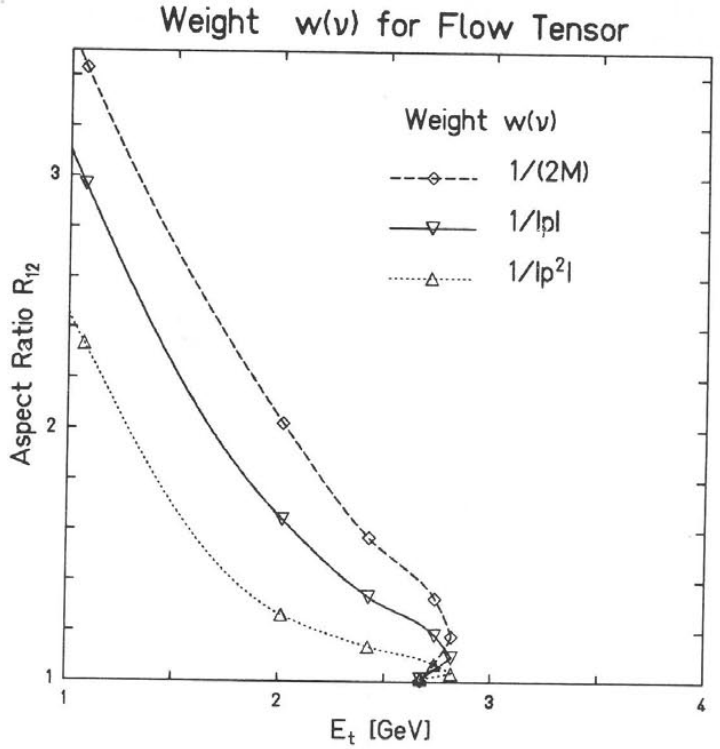

Fig. III.36. Dependence of the aspect ratio R_{12} vs. the transverse energy E_t on the various weights $w(\nu)$ used in the flow analysis.

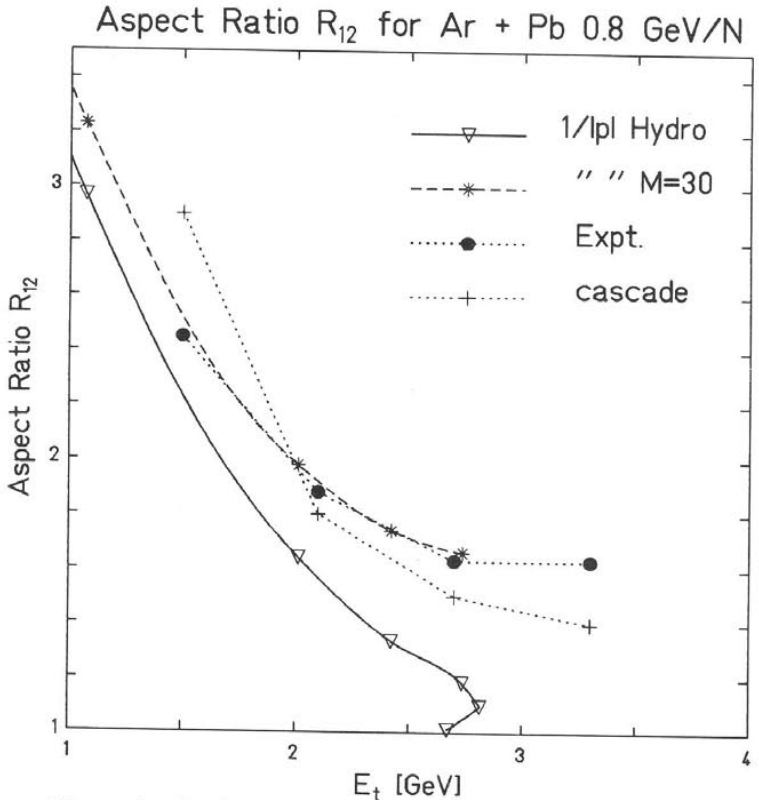

Fig. III.37. Comparison of R_{12} vs. E_t (see previous figure) as obtained from fluid dynamics with and without finite multiplicity distortions [Gra84] for the reaction Ar (0.8 GeV/nucleon) + Pb with the data [Str83].

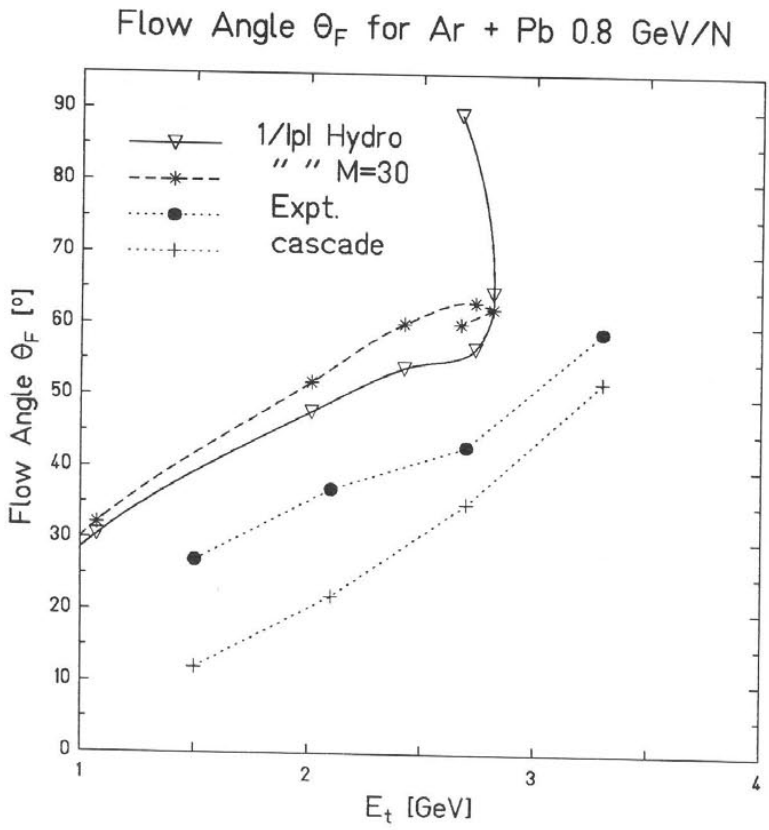

Fig. III.38. Flow angle vs. transverse energy as obtained from the relativistic fluid dynamical model [Gra84] with and without finite multiplicity distortions as compared to the data and cascade calculations [Str83] for the reaction Ar (0.8 GeV/nucleon) + Pb.

θ_F values as a function of E_t as determined by hydrodynamics (solid curve). The values corrected for finite multiplicities [Dan84] of 30 (dashed line) are also shown. In addition, the cascade and experimental values are shown [Str83]. With increasing E_t, i.e. decreasing b, the flow angle increases, i.e. shows more sidewards flow, and R_{12} decreases, which in this case indicates more isotropy. Hydrodynamics exhibits the largest flow angles, while the experimental data lie between the hydro and cascade results. The flow angle distribution for data, cascade and fluid dynamics are compared in fig. III.39.

A further indication of hydrodynamical behavior can be seen in fig. III.40 which shows the mean longitudinal versus mean transverse momentum per event. Events which lie on the dotted line may indicate isotropy. However, events with a collective flow may also exhibit the same transverse as longitudinal momenta and hence may lie on the dotted diagonal line. The only direct signature for strong transverse flow in this plot is due to events which lie above this line. This is the case for central collisions, $b < 4$ fm, in the hydrodynamic calculation. Also the experimental data [Str83] lie above this line once high-E_t events are selected. However, it is not clear if this is an indication for strong transverse flow or only the result of a bias due to the high E_t sampling [Str83]. The high-E_t cascade events [Str83] only approach the diagonal, which in this case still means a forward peaking because of the sampling bias.

Unfortunately an improved quantitative comparison is not possible at this stage. On the one hand,

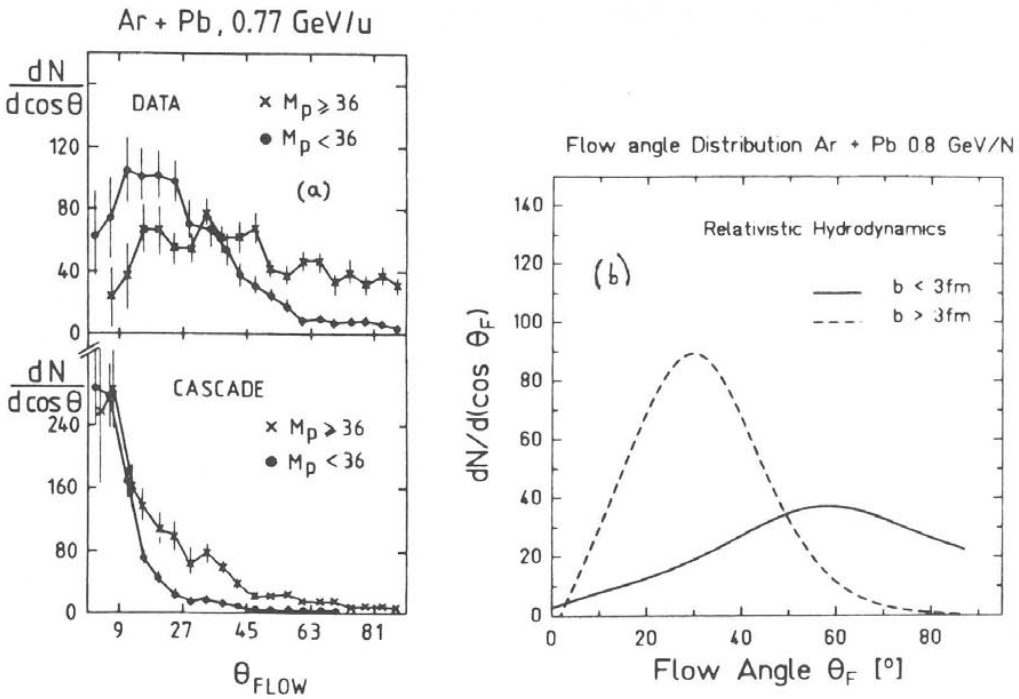

Fig. III.39. Comparison of the flow angular distribution obtained experimentally for the reaction Ar(0.8 GeV/nucleon) + Pb and the cascade predictions [Ren84] to the predictions of the relativistic one fluid model [Gra84].

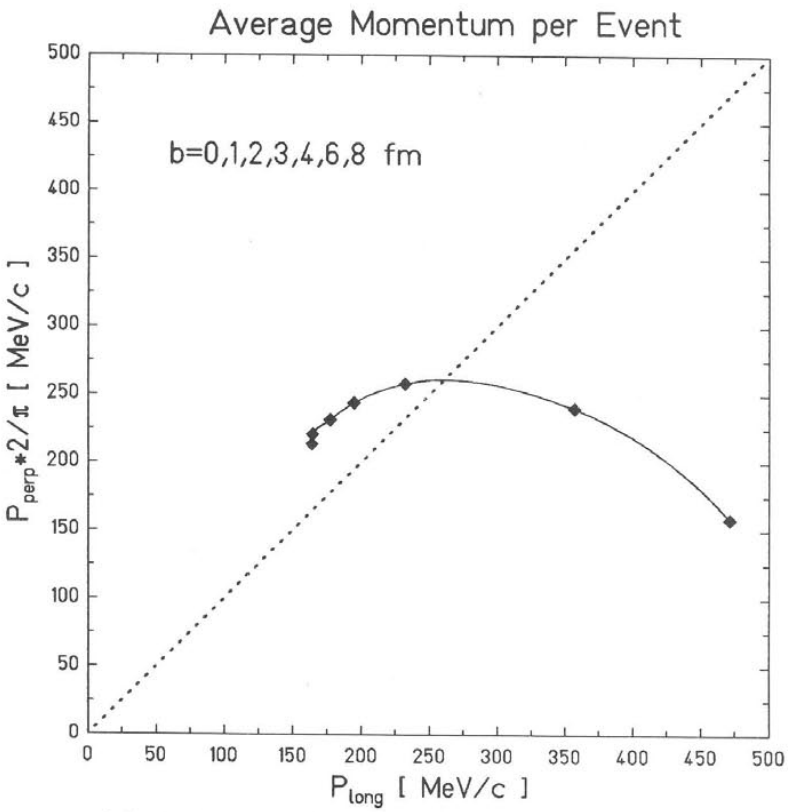

Fig. III.40. Average c.m. momentum calculated with the relativistic one fluid model for the reaction Ar((0.8 GeV/nucleon) + Pb[Gra84] as a function of impact parameter b given in the figure (corresponding to the squares from left to right).

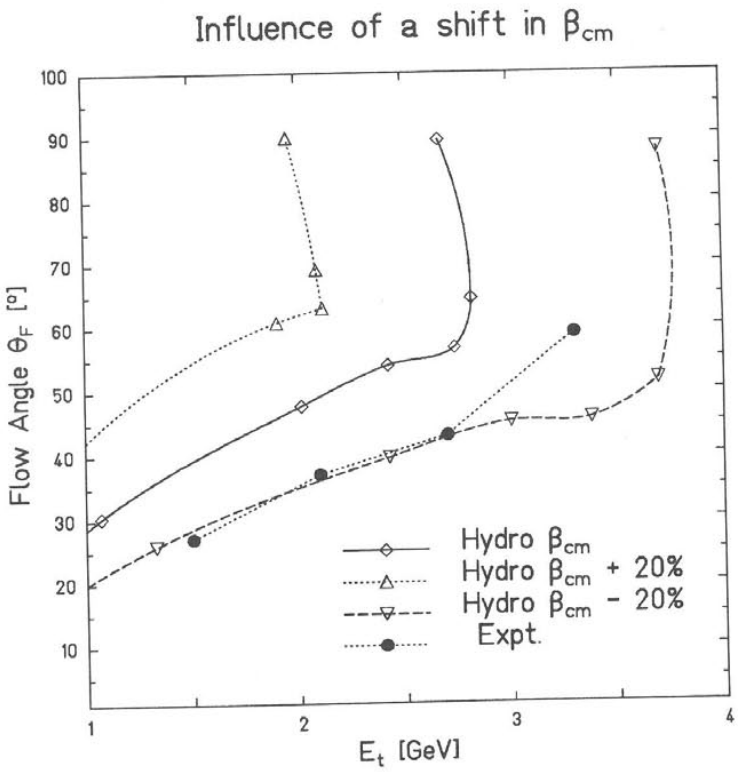

Fig. III.41. Influence of a rather slight shift of $\beta_{c.m.}$ on the resulting flow angles. The relativistic fluid dynamical calculations [Gra84] are compared to the experimental data [Str83]. This ambiguity for asymmetric systems is best avoided by analysis in a prescribed Lorentz frame, say the nucleon–nucleon center of mass [Mol85].

the finite particle effects are only treated approximately in the hydrodynamical calculations. On the other hand, the varying participant c.m. velocity of this asymmetric system, particularly in combination with the restriction to the forward hemisphere, leads to problems with the specification such quantities as E_t and the flow tensor.

A small change in the c.m. velocity, which is experimentally determined for each event, results in a dramatic displacement of the event in the $p_\perp, p_\parallel$ plane. A small increase of $\beta_{c.m.}$ for example, causes particles with essentially transverse momenta to be displaced from the forward hemisphere. Thus the effective E_t of the event is reduced. In addition, the longitudinal momentum components of the remaining forward particles are reduced which in turn changes both flow angle and aspect ratio. Thus both axes of the corresponding figures are distorted. This effect is demonstrated in fig. III.41 where the variation of θ_F (about a factor of 2!) with a $\pm 20\%$ change in $\beta_{c.m.}$ is depicted.

The best solution we see is to perform the analysis in the n–n c.m. system which is well defined (see the VUU analysis below).

III.3.8. Microscopic analysis of collective flow – Indication for a stiff EOS

The quantitative confirmation of the longstanding predictions of the collective sidewards flow [Sch74, Stö80] discussed in the previous section established clearly the formation of highly compressed nuclear matter.

On the other hand, although the key mechanism for the investigation of the properties of high density matter has been identified, the problem remains to extract the nuclear equation of state, in particular the compression energy, from the flow data. This can in principle be accomplished via a detailed comparison with the hydrodynamic model predictions for different equations of state and different transport coefficients. However, we have seen in the previous section that there is a substantial non-equilibrium contamination of the data, i.e. direct (knock-out) nucleon–nucleon scattering, etc. It has been shown that it is not entirely clear how to subtract this contamination from the data. Therefore, in order to perform a quantitative extraction of the compression energy from the data, we will in the following return to the microscopic approaches discussed and applied above, in particular the Newtonian Force Model and the VUU approach [Mol85], and re-analyze the flow data.

In the Newtonian Force Model the computations are stopped after $t = 30$ fm/c, after which the flow results are constant. The evolution of a collision at $b = 3$ fm impact parameter is shown in fig. II.1. The resulting sidewards flow can clearly be seen. Note that the average deflection angle of the center of mass of projectile and target nucleons, respectively, is approximately equal to the average calculated flow angle. This associates a simple meaning to the flow concept. The demonstrated strong correlation between configuration space and momentum space can be attributed to the repulsive short range component of the nucleon–nucleon potential.

The individual collisions are again analyzed by diagonalizing the kinetic energy flow tensor [Gyu82]

$$F_{ij} = \sum_{\nu} p_i(\nu)\, p_j(\nu)/2m(\nu) \tag{III.32}$$

where the sum is over all charged particles in a given event. By diagonalizing this tensor, the flow angle θ_F is obtained for each event. The distribution of flow angles $\mathrm{d}N/\mathrm{d}\cos\theta_F$ for the NFM model is presented in fig. III.42 for various impact parameter intervals. The qualitative behavior of the flow pattern in the NFM model is as in the NFD model: the flow angle θ_F rises smoothly from 0° at large impact parameters to 90° at $b = 0$ fm. However, the contribution of zero impact parameter collisions to the observable cross sections is negligible. Thus a finite range of impact parameters is sampled to compute the angular distributions of the flow angles, $\mathrm{d}N/\mathrm{d}\cos\theta_F$, which is to be compared to the experimental data of the GSI–LBL collaboration.

The distribution of flow angles was computed taking into account the formation of fragments via a generalized coalescence model [Mol84a]. It is found that one obtains roughly the same flow distribution by doing the flow analysis with protons only (no clustering), with clustering (protons only), or by counting all particles obtained with the coalescence model.

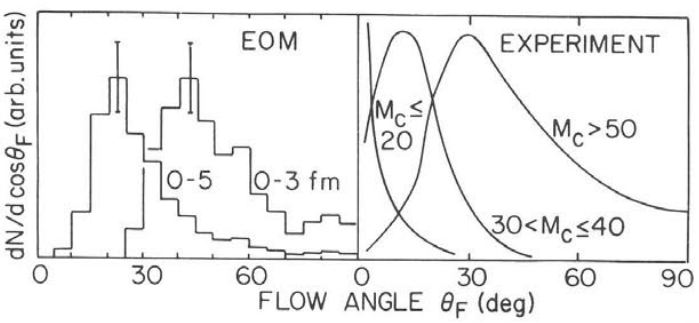

Fig. III.42. Kinetic energy flow angle distributions for Nb (400 MeV/nucleon) + Nb in the Newtonian Force Model compared to the experimental data [Mol84a].

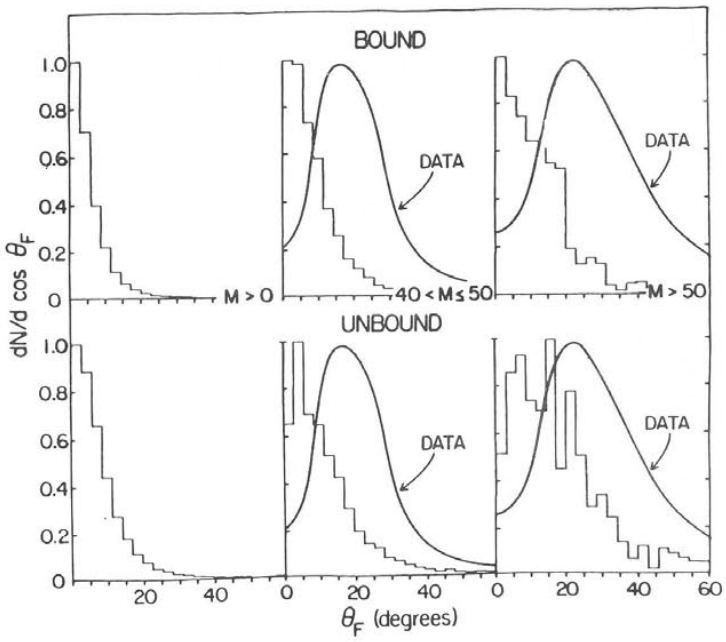

Fig. III.43. The bound and unbound Cugnon cascade compared to the experimental data for Nb (400 MeV/nucleon) + Nb in various multiplicity bins [Mol85].

As discussed above, fig. III.34 shows the experimental data for the Nb(400 MeV/N) + Nb case as compared to the predictions of the intranuclear cascade, and fluid dynamical calculations. The data exhibit non-zero average flow angles once high multiplicity, i.e. small impact parameter collisions, are selected. This is in contrast to the intranuclear cascade calculation (using the Yariv Frankel and Cugnon approaches), which yields zero flow angles even at the highest multiplicities (also see fig. III.43).

The microscopic NFM model, on the other hand, predicts peaks in the angular distributions of the flow angles. The peak shifts to larger angles with increasing multiplicity, just as the fluid dynamic model. This is in qualitative agreement with the experimental data. The physical difference between the INC model and the NFM approach, which leads to such distinct predictions can be traced back to the different treatments of the NN collision process. The INC applies a stochastic 4π scattering at the point of closest approach of straight line trajectories; this allows for substantial transparency. In contrast, the repulsive short range component in the NN potential used for the NFM approach is a soft core and thus effectively results in an excluded volume effect. The nuclei are not as transparent and easily compressible as in the INC. This causes incident nucleons to be deflected away from zones of high density, i.e. small interparticle separations, towards sidewards angles.

Let us now return to the VUU theory, which also predicts finite flow angles [Kru85a, Mol84, 85] and re-analyze the flow data. Let us study the flow angle as a function of time. For example, in Nb (1050 MeV/nucleon) + Nb, at $b = 3$ fm, the flow angle reaches a maximum at $t = 14\,\mathrm{fm}/c$ (see fig. III.44). The compression or density of nuclear matter reaches its maximum value at $5\,\mathrm{fm}/c$ (fig. III.45): it takes a finite amount of time for the equilibration of the momentum distribution to occur.

As a function of energy, the density probed in heavy ion collisions is very similar in Au + Au (see fig. III.46), Nb + Nb, or Ar + KCl collisions. What is important for the maximum density probed is not the atomic number, but the EOS: higher densities are achieved with softer equation of states. Notice that

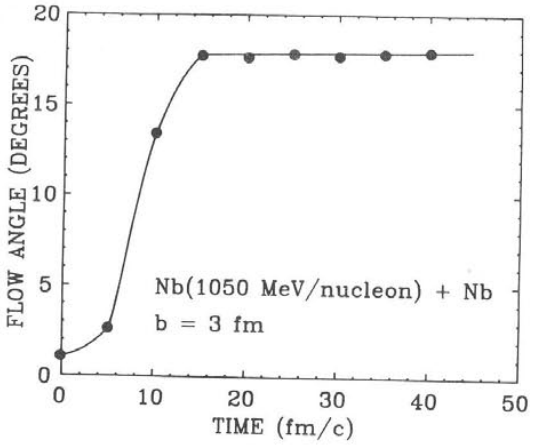

Fig. III.44. The average flow angle for Nb (1050 MeV/nucleon) + Nb at $b = 3$ fm versus time in the VUU approach [Mol85].

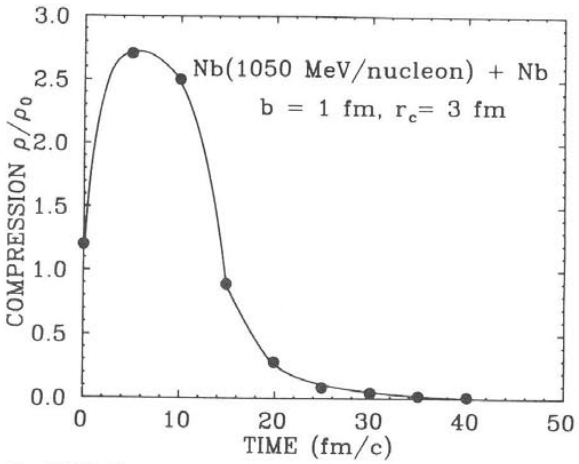

Fig. III.45. The corresponding time dependence of the compression for Nb (1050 MeV/nucleon) + Nb at $b = 3$ fm in a central region of radius 2 fm shows that the flow angle can yield information about the high density stage [Mol85].

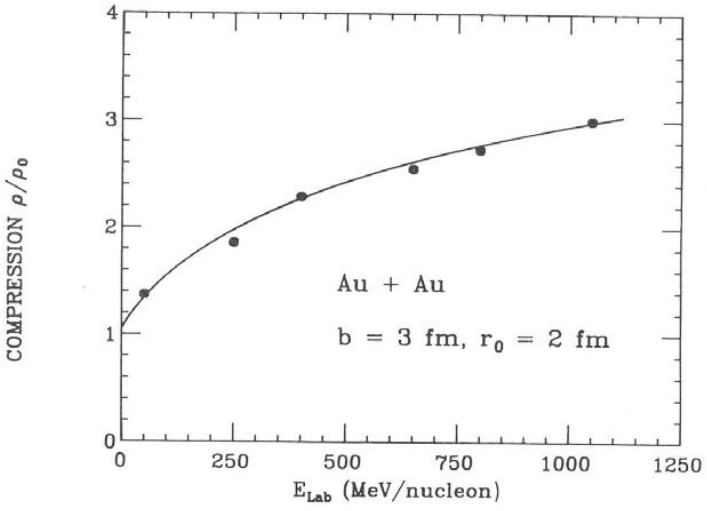

Fig. III.46. Maximum density in the center of mass frame for Au + Au collisions at $b = 3$ fm in the VUU approach [Mol85].

the densities probed with the VUU theory are much less than those reached with the less realistic intranuclear cascade model. The most important result of this section is, however, the strong dependence of the flow angle on the EOS.

The density probed is related to the flow angle for a given system via the EOS. A softer equation of state results in lower peak flow angles (fig. III.47). Hence, the flow data indicate again a stiff EOS [Kru85a], which is the only one which results in the required large flow angles.

How does the peak flow angle vary as a function of the bombarding energy? At fixed impact parameter ($b = 3$ fm), the flow angle reaches a maximum value at 400 MeV/nucleon and then does not change further as the collision energy increases (fig. III.48). There is however a very strong effect due to the atomic number (fig. III.49) at fixed energy $E = 400$ MeV/nucleon. This is easily understood: even though these different symmetric systems probe the same densities, there are much more collisions for

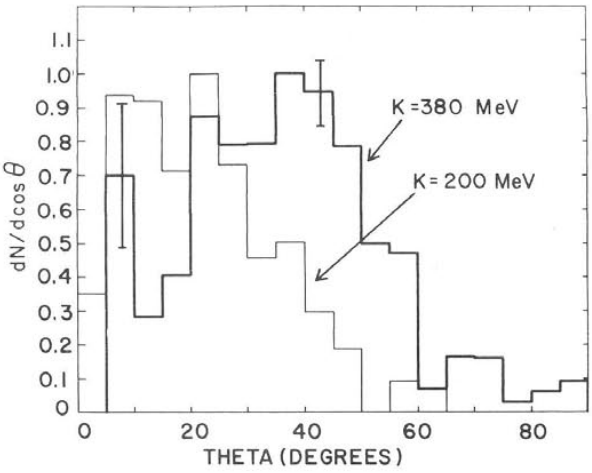

Fig. III.47. Effect of the compressibility on the flow angle distribution for Nb (400 MeV/nucleon) + Nb at $b = 1$ fm in the VUU approach [Kru85a]: the flow angle indicates a stiff nuclear equation of state.

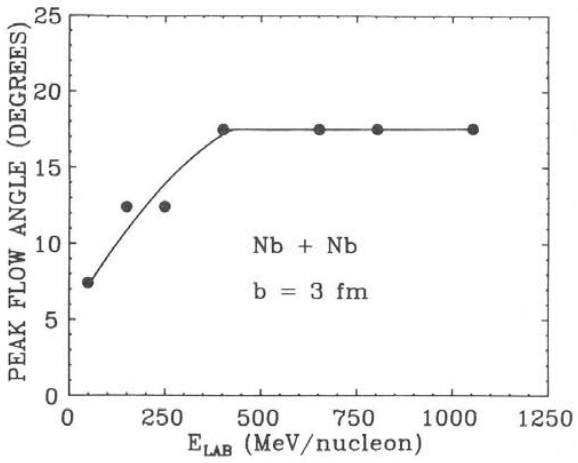

Fig. III.48. Peak flow angle versus bombarding energy from a VUU calculation for Nb + Nb at $b = 3$ fm [Mol85].

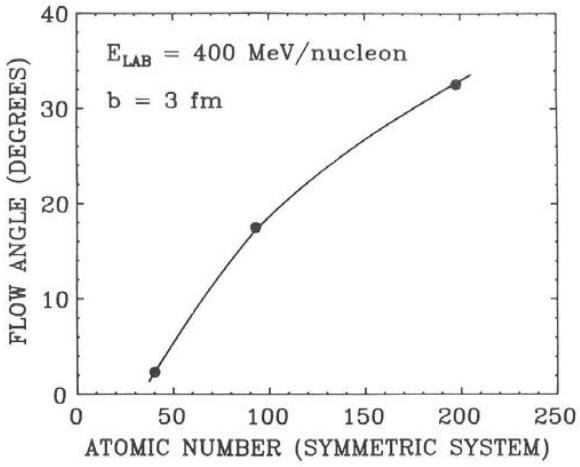

Fig. III.49. Peak flow angle in the VUU model for $E = 400$ MeV/nucleon at $b = 3$ fm strongly depends on atomic number due to the increased number of collisions [Mol85], in agreement with recent Plastic Ball data [Rit86].

the higher atomic numbers. The collective flow thus comes about as an interplay between the collision term and the EOS in the VUU theory. One finds similar results for the peak flow angle in Au + Au versus energy (fig. III.50) at $b = 3$ fm except that the maximum flow angle is now twice as large than for Nb + Nb (fig. III.48) [Mol85]. This is in agreement with the recent Plastic Ball data on Au + Au [Rit86].

Asymmetric collisions in the VUU approach present results consistent with but somewhat different from the above. One sees from fig. II.12 that in order to detect the collective sidewards flow of nuclear matter one needs to look at the projectile hemisphere $p_z < 0$ in momentum space. An asymmetry here is evidence of collective flow; this is easily observed at the intermediate impact parameter $b = 5$ fm in fig. II.12. Observe that the flow of nucleons in momentum space is correlated with a flow in configuration space, as is the case also for symmetric systems. This was discussed already in the previous section.

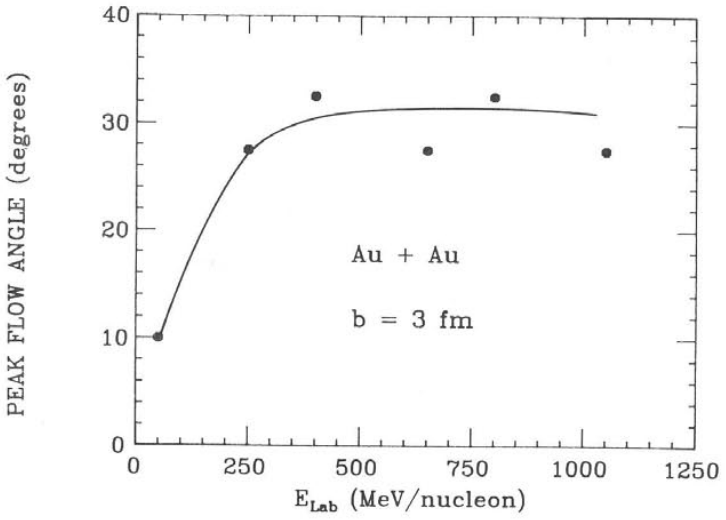

Fig. III.50. Peak flow angle versus energy for Au + Au at $b = 3$ fm from the VUU approach [Mol85].

Let us compare now the predictions of the VUU approach to the data of the GSI–LBL streamer chamber group presented above. The experimentalists analyzed their data using the momentum flow tensor:

$$P_{ij} = \sum_{\nu} [p_i(\nu)\, p_j(\nu)/\mathrm{abs}(p(\nu))] \Big/ \sum_{\nu} \mathrm{abs}(p(\nu))\,. \tag{III.33}$$

The data analysis proceeds on an event by event basis in a rather non-trivial way (see section III.3.7). First, only charged particles are used. Then the center of mass velocity for each event is computed from the momenta of all charged particles with transverse momenta per nucleon greater than the Fermi momentum. Then only the forward hemisphere of this participant center of mass frame is analyzed. Their results are shown again in fig. III.51a. We compare in fig. III.51b the corresponding predictions of the Vlasov–Uehling–Uhlenbeck theory. Both in theory and experiment a broad bump is observed in the angular distribution of flow angles for near central collisions, while a rather sharp peak occurs at 15–30 degrees for the medium impact parameters, i.e. intermediate multiplicity events. This contrasts strongly with the results of intranuclear cascade calculations, which exhibit forward peaked angular distributions independent of impact parameter as well for asymmetric as for symmetric collisions. The peak seems also to be located at somewhat smaller angles than obtained in fluid dynamics, see fig. III.39.

The flow analysis has also been done in the more rigidly defined nucleon–nucleon center of momentum system with the coalescence invariant kinetic energy flow tensor. The analysis is also restricted to the projectile momentum hemisphere $p_z < 0$ since this will avoid the distortion of the event shape by the large number of target spectators at rather small momenta and thus best reflect the flow of the participant nucleons. We see in fig. III.51c that the flow distribution changes its characteristics in particular for the high multiplicity events. One now sees a distribution skewed towards 90° for the small impact parameters, while the peak remains near 20° for the intermediate impact parameters. This is similar to the results for symmetric systems; the peak of the flow angle distribution decreases with increasing impact parameter.

In fig. III.52 the standard kinetic energy flow distributions are compared for individual impact parameters to the novel transverse momentum analysis of Danielewicz and Odyniec [Dan84] that

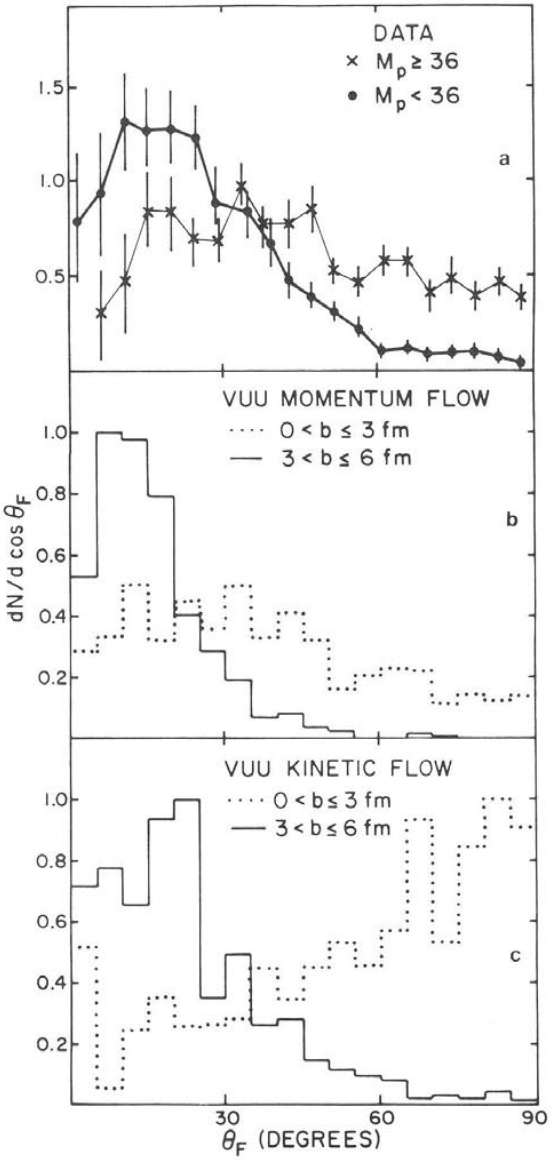

Fig. III.51. Flow angle distributions for Ar (770 MeV/nucleon) + Pb for (a) the experimental data with high and low multiplicity cuts using the momentum flow tensor [Ren84]; (b) corresponding predictions of the VUU theory; and (c) a standard kinetic energy flow analysis done in the nucleon–nucleon center of momentum frame using only the projectile momentum hemisphere [Mol85].

was discussed extensively in connection with fluid dynamic results above. It provides a sensitive test for collective flow and its dependence on the nuclear equation of state even in light systems [Mol85a]. The transverse momentum spectrum $p_x(y)$ is analyzed, remember that here

$$y = \tfrac{1}{2}\ln(E + p_{\text{par}})/(E - p_{\text{par}}) \tag{III.34}$$

is the rapidity, E is the total energy of the fragment, and p_{par} is the momentum in the beam direction. Note that in the simulations shown here the projectile has $p_{\text{par}} = p_z > 0$; in the configuration

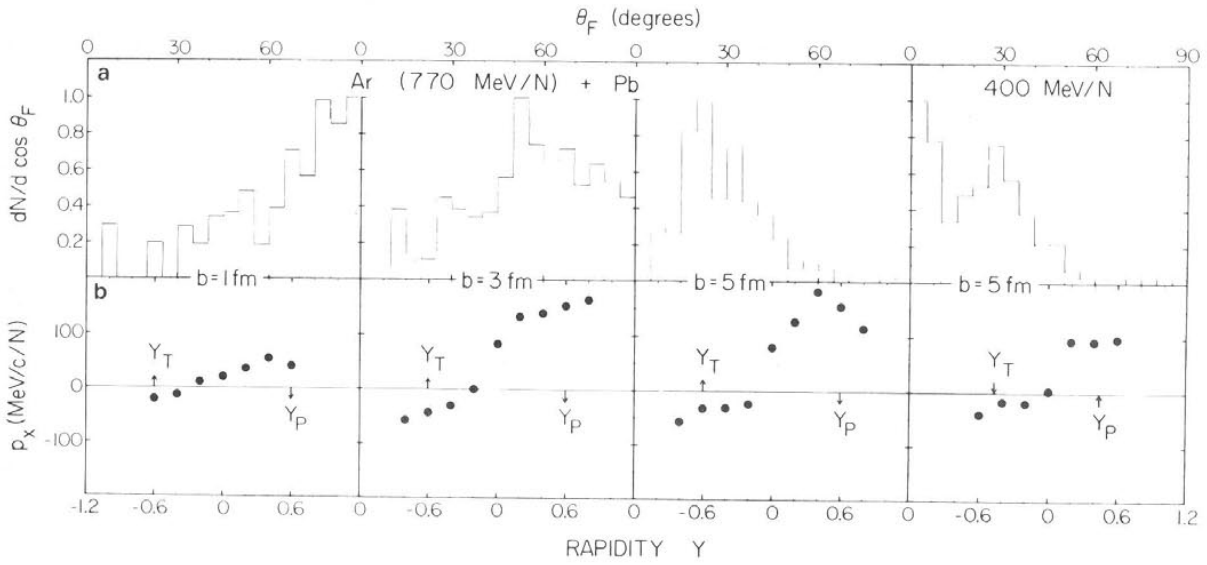

Fig. III.52. VUU predictions for two different methods of detecting collective flow are shown for Ar + Pb: (a) the standard kinetic energy flow analysis in the NN center of momentum frame is done on the forward hemisphere for $b = 1$, 3 and 5 fm and (b) the transverse momentum analysis is shown at the same impact parameters [Mol85].

and momentum space plots shown above the axis have been flipped for ease of viewing. This technique has also been used to predict the presence of collective flow for ^{16}O (600 MeV/N) + ^{16}O within the time dependent Dirac equation approach [Cus85] (see fig. III.57).

As is evident from fig. II.12, the flow angle approaches its asymptotic value rather rapidly; indeed at $b = 3$ fm, the final flow angle distribution is established in less than 20 fm/c. At $b = 1$ fm, the flow angle distribution is skewed to 90°, i.e., the projectile momentum hemisphere exhibits sidewards peaking as is evident from fig. III.52; a significant number of particles are thrust to the side perpendicular to the beam axis. A broad peak around 55° is observed at $b = 3$ fm; the flow angle begins to become well defined. For $b = 5$ fm, there is a clear peak at 20–30 degrees. Thus it is only at the intermediate impact parameters that the flow is evident by a sharp peak in such asymmetric systems. Part of the reason why the peak is not so pronounced at lower impact parameters is statistical: the projectile hemisphere contains substantially fewer fragments in the final state in an Ar + Pb collision than in a Nb + Nb collision.

In the transverse momentum plots, much the same behavior is seen. However, here the analysis is not restricted to the forward hemisphere in momentum space. Summation over p_x and division by the number of protons in each rapidity bin shows very little flow effects in the target rapidity region, which is dominated by target spectator matter. At $b = 1$ fm, p_x/N is about 50 MeV/(c N) at projectile rapidity, $y_p = 0.60$, whereas at target rapidity, $y_T = -0.60$, p_x amounts to only 25 MeV/(c N). The flow at $b = 3$ fm is particularly pronounced in this method of analysis: $p_x(y_P) = 150$ MeV/(c N) whereas $p_x(y_T) = 40$ MeV/(c N). At $b = 5$ fm, we have much the same result as at $b = 3$ fm. Note that in the massive system studied here the transverse momentum transfer (bounce-off effect) is larger than in lighter systems at higher energies – 100 MeV/(c N) have been observed for the system Ar (1.8 GeV/N) + KCl (fig. III.55).

Effects of the nuclear equation of state have also been looked for by varying the compressibility from $K = 380$ MeV to $K = 200$ MeV at $b = 1$, 3 and 5 fm. At the lower impact parameter, the broad distribution prevents any statistically significant difference from being seen. At the intermediate impact

parameter, one sees a small shifting of the flow angle peak to the smaller angles as the compressibility decreases; this is consistent with, but less dramatic than, what we have found for symmetric systems. Note that one sees a great difference if $K = 0$ MeV, i.e., the cascade model is used; then the distributions are peaked at zero degrees for all impact parameters. An equation of state with compressional energy seems essential to qualitatively reproduce the data; but asymmetric systems appear to be less sensitive to the details of the equation of state than symmetric collisions. Furthermore, one can look for quantal effects by turning off the Pauli principle at $b = 3$ and 5 fm. No strong effects are seen. This is somewhat of a surprise in view of the strong effect we see in the symmetric case and the fact that about 50% of the collisions are Pauli blocked even at this high energy. However, this may perhaps be understood by the fact that many of the blocked collisions are between nucleons in the same nucleus, not between nucleons in the compression zone.

Let us also study the same system at a lower energy 400 MeV/N (see fig. III.52). The kinetic energy flow angle distribution becomes more forward peaked at fixed impact parameter $b = 5$ fm. The transverse momentum transfer $p_x(y_P)$ decreases to 100 MeV/(c N). The similar system Ar (92 MeV/N) + Au shows what happens in an event by event analysis as the energy is decreased further: the flow distributions at $b = 2$, 3 and 4 fm impact parameter become very broad; the transverse momentum at beam and target rapidities is zero to within 10 MeV/(c N). At still lower energies, the transverse momenta spectra are inverted as the attractive part of the nuclear potential becomes dominant: the bounce-off caused by the short range repulsion at high density is converted into the negative angle deflection known from TDHF calculations in this energy region and from experimental data.

The transverse momentum for symmetric systems Nb + Nb (fig. III.53) and Au + Au (fig. III.54) is a strong function of energy. At $b = 3$ fm the transverse momentum $p_x(y_P)$ rises from negative or zero values for $E < 100$ MeV/nucleon to 140 to 160 MeV/(c nucleon) at 1050 MeV/nucleon for Nb and Au

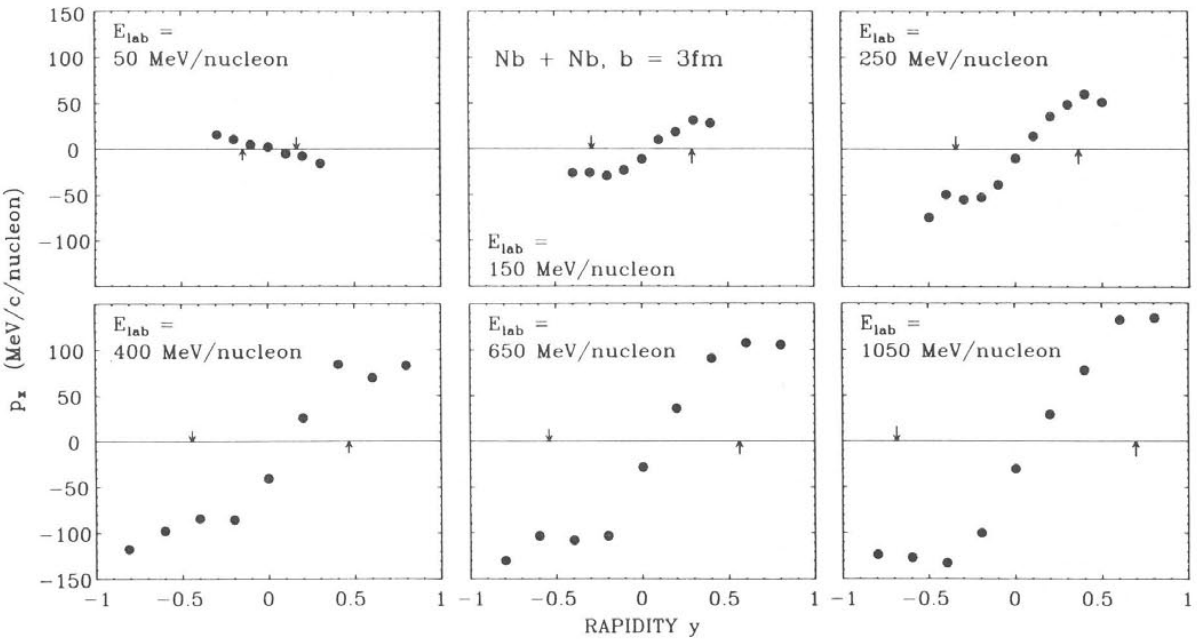

Fig. III.53. Transverse momentum spectra for Nb + Nb at $b = 3$ fm versus energy in the VUU theory [Mol85].

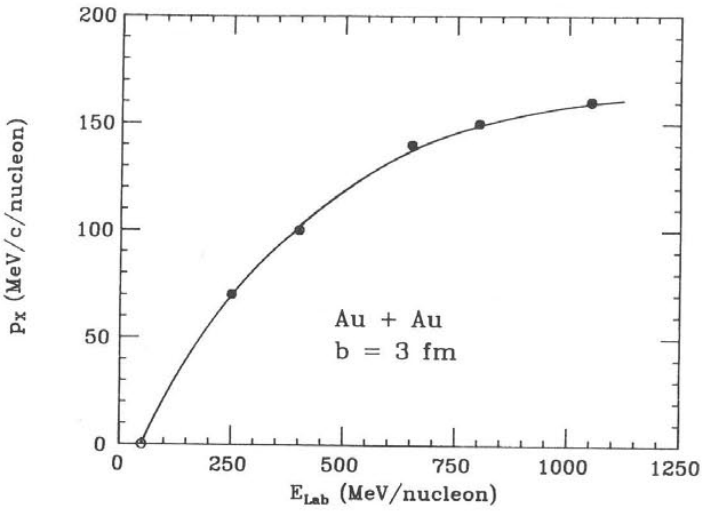

Fig. III.54. Transverse momentum at projectile rapidity for Au + Au at $b = 3$ fm versus energy in the VUU theory [Mol85].

systems, respectively. The bounce-off increases dramatically with energy but only slightly with atomic number. The absolute value of $p_x(y_P)$ in the VUU approach is comportable to the values obtained in the fluid dynamical model, see fig. III.23.

III.3.9. More evidence for a stiff nuclear equation of state from the transverse momentum analysis

For light systems and high energies flow effects are not observed when the standard kinetic energy flow analysis is used. In fact, the experimental flow angular distributions for the reaction Ar(1800 MeV/nucleon, $b < 2.4$ fm) + KCl are peaked at zero degrees as the cascade model predicts. But here also the Vlasov–Uehling–Uhlenbeck approach, which, as we have just seen, does predict finite flow angles for heavier systems at lower energies, does not yield any observable sidewards maxima in the flow angle distributions; even less so can we distinguish between hard and medium equations of state when the standard kinetic energy flow tensor analysis is used: all flow angle distributions are peaked at zero degrees [Mol85a]. Therefore, one might be tempted to hastily conclude that flow effects do not occur for light systems.

However, Danielewicz and Odyniec have recently shown that their novel transverse momentum analysis technique provides a much more sensitive test for collective flow: Danielewicz and Odyniec have been able to determine the scattering plane in the experimental data by controlling the finite multiplicity distortions carefully. They have tested their method by subjecting events generated via the intranuclear cascade model, i.e. events where the actual reaction plane has been given, to their procedure for determining the reaction plane from data and find good agreement. In the following we compare the first experimental data in the extracted scattering plane to the theoretical results in the given $(x–z)$ scattering plane.

Danielewicz and Odyniec detected collective flow effects in the streamer chamber data for Ar(1800 MeV/nucleon) + KCl using this technique (see fig. III.55). There is a transverse momentum

accumulation at both the projectile and target rapidities $y = \pm 0.86$ in the center of momentum frame. They report that the collective flow effects are weaker than in the hydrodynamic model, but much stronger than in the cascade (see fig. III.55). It is important to point out that the intranuclear cascade model fails to reproduce the data, even though it appeared to be consistent when the kinetic energy flow analysis had been applied. The highly increased sensitivity of this new technique has more recently been used to predict the presence of collective flow for O (600 MeV/nucleon) + O within the context of the time dependent Dirac equation with relativistic mean field dynamics, see figs. III.56 and III.57 [Cus85].

The transverse momentum analysis technique has also been applied [Mol85] to the Vlasov–Uehling–Uhlenbeck results for the reaction Ar(1800 MeV/nucleon, $b < 2.4$ fm) + KCl studied experimentally. One finds that the peak in the transverse momentum spectrum $p_x(y)$ depends linearly on the nuclear equation of state: the cascade model predicts $p_x^{\max} \approx 25$ MeV/(c nucleon) (fig. III.55), the medium equation of state in the Vlasov–Uehling–Uhlenbeck approach predicts $p_x^{\max} \approx 50$ MeV/(c nucleon) (fig. III.55d), and the stiff equation of state yields $p_x^{\max} \approx 100$ MeV/(c nucleon) (fig. III.55c). Only the latter is in agreement with the data.

This result further supports the finding that the stiff equation of state reproduces best the collective flow at lower energies, the pion yields observed in the streamer chamber at 1800 MeV/nucleon and also at lower energies, down to 360 MeV/nucleon (fig. III.12). It is important that this equation of state (see fig. II.3) agrees also rather well with the one extracted from the pion data via other procedures [Sto82, San85, Hah85], thus offering the fourth independent clue on the stiffness of the nuclear matter equation of state [Mol85].

Although these results should not be viewed as the final word in our search for the nuclear equation of state at density 2–4, we seem to have a first glimpse on this basic bulk property of dense nuclear matter.

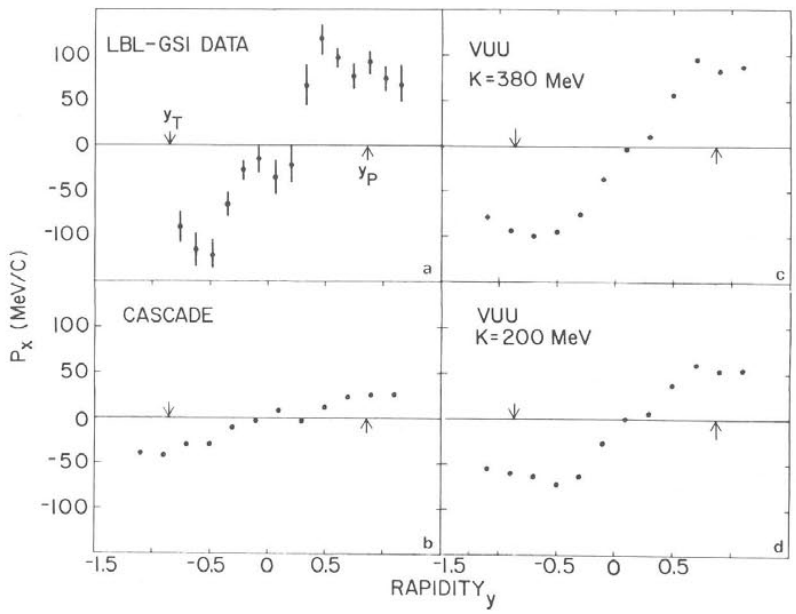

Fig. III.55. Transverse momentum spectra for Ar (1800 MeV/nucleon) + KCl for the experimental data (a), intranuclear cascade (b), and the VUU approach with hard (c) and soft (d) equations of state. The data again indicate a stiff nuclear equation of state [Mol85].

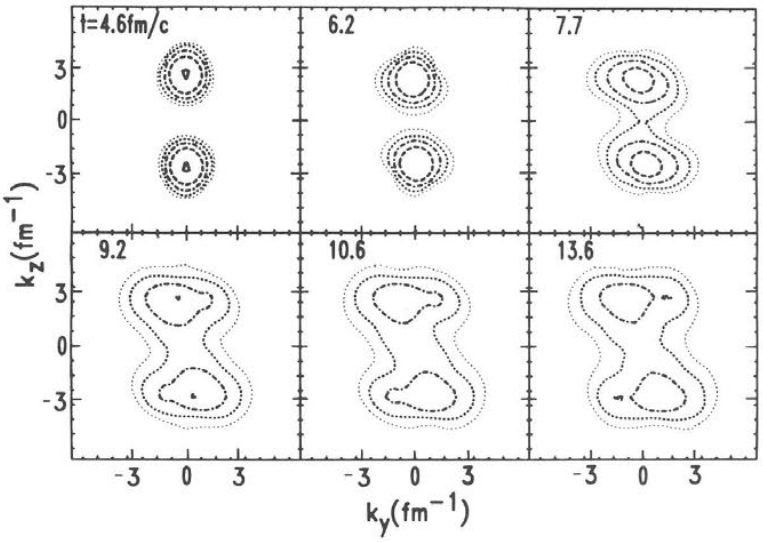

Fig. III.56. Momentum space density contours for the reaction ^{16}O (600 MeV/nucleon) + ^{16}O As obtained as a function of time from the solution of the time dependent Dirac equation (TDDE). The build-up of transverse momentum transfer is observed at $t > 7$ fm/c [Cus85].

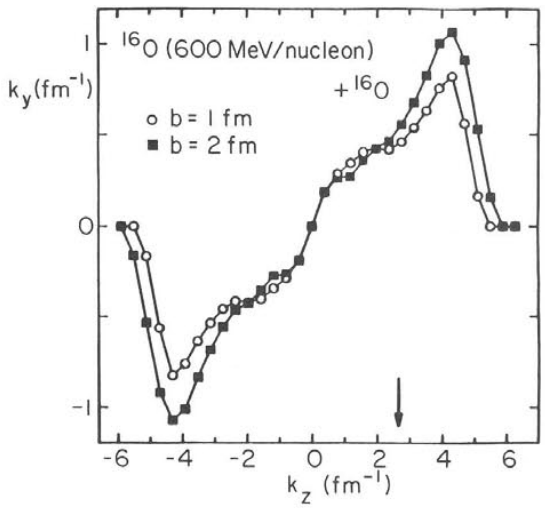

Fig. III.57. Projection of the in-plane transverse momentum per nucleon, k_y, versus the longitudinal momentum, k_z, as obtained from the TDDE approach [Cus85]. The results agree qualitatively with the data obtained by the GSI–LBL streamer chamber collaboration at higher energies and with more massive nuclei [Dan85].

IV. Creation of the quark-gluon plasma at ultra-relativistic energies – Space-time evolution of the high energy density region

The possibility of creating an entirely new form of matter, the deconfined quark-gluon plasma, in the laboratory has spurred a tremendous activity, both theoretical and experimental, in the high energy and nuclear community during the last few years [QM79, QM80, QM82, QM83, QM84, see also Cle85]. We